Global Wind Stress and Sverdrup Circulation from the Seasat Scatterometer

DUDLEY B. CHELTON AND ALBERTO M. MESTAS-NUÑEZ

College of Oceanography, Oregon State University, Corvallis, Oregon

MICHAEL H. FREILICH

Jet Propulsion Laboratory, California Institute of Technology, Pasadena, California

ABSTRACT

Three months of vector wind observations from the Seasat-A satellite scatterometer (SASS) are used to construct gridded fields of monthly average wind stress and wind stress curl over the global ocean. These fields are examined to identify features either poorly resolved or not present in wind stress fields constructed from conventional data. Particular attention is focused on the spatial structures in the high southern latitudes and the tropical regions. The SASS wind stress fields are compared globally with the Hellerman and Rosenstein climatological monthly average surface wind stress fields and with monthly averages of wind stress computed from contemporaneous 1000 mb wind analyses produced by the National Meterological Center.

The potential for satellite scatterometry improving the present knowledge of the global wind stress field and making important contributions to ocean modeling is demonstrated by comparison of global maps of the Sverdrup circulation computed from 3-month average SASS and Hellerman and Rosenstein climatological wind stress curl fields. Except for the region south of about 35°S, the two estimates of Sverdrup circulation are generally very similar. The transports of the western boundary currents calculated from the climatological wind stress fields are consistently higher because the drag coefficient used by Hellerman and Rosenstein is too large by approximately 19%. In the Antarctic Circumpolar Current region, the difference between the two estimates of zonal transport is very large, even disagreeing in direction in the region south of Australia and New Zealand. Historical hydrographic data suggest a tendency, albeit less extensive, for the westward Sverdrup transport indicated by the SASS data, suggesting the possibility of deficiencies in the climatological wind stress fields.

1. Introduction

Recent advances in computer modeling of ocean circulation have made possible high resolution global simulations of the ocean response to wind forcing. Bryan and Lewis (1979) developed an early coarse-resolution global ocean circulation model forced by climatological annual mean wind stress from Hellerman (1967). Semtner and Chervin (1988) recently presented the first eddy-resolving global simulation, based on climatological annual mean wind stress forcing from Hellerman and Rosenstein (1983); seasonally forced simulations are presently under development. The wind stress fields used to force these global models were derived from ship observations of winds over the past century. These ship observations are heavily biased in favor of the Northern Hemisphere and along standard shipping routes; they are conspicuously absent over most of the middle and high latitudes of the Southern Hemisphere and much of the tropics. The inhomogeneous distribution of ship observations thus

raises concern over the quality of existing estimates of climatological mean seasonal winds over a considerable fraction of the world oceans. Accurate fields of wind forcing are essential if realistic model simulations of ocean circulation are to be achieved.

Satellite scatterometry promises to improve the present knowledge of the global wind field. To date, the only satellite scatterometer has been the Seasat-A Satellite Scatterometer (SASS) which measured near-surface winds over the global ocean from 7 July through 10 October 1978. This situation will soon change with the launches of the European Space Agency scatterometer onboard the ERS-1 satellite (expected launch date in early to mid-1991) and the NASA scatterometer (NSCAT) onboard the Japanese ADEOS satellite (expected launch date in 1995). Global wind fields estimated from these scatterometers will be a key element of large-scale ocean circulation studies of the 1990s. To gain an appreciation of the impact that these future scatterometer data will have on ocean modeling, we analyze here global surface wind stress fields estimated from the three months of SASS data.

Since the time of the Seasat mission, there have been few applications of the SASS data, in part because the relatively short 3-month dataset restricts the range of

Corresponding author address: Dr. Dudley Chelton, College of Oceanography, Oregon State University, Oceanography Admin. Bldg. 104, Corvallis, OR 97331-5503.

geophysical problems that can be addressed. A second and perhaps more restricting limitation has been the inherent difficulty in selecting a unique wind direction from the multiple vector solutions produced from each SASS observation. Recently, three months of SASS vector wind observations, with the directional ambiguities removed, have been made available by R. Atlas at the Goddard Space Flight Center (GSFC) Laboratory for Atmospheric Sciences. The quality of this wind dataset is extensively evaluated in Atlas et al. (1987) and in a companion paper to this study, Chelton et al. (1989), by comparison with 14 days of SASS vector winds for which the directional ambiguity had been subjectively removed by trained meteorologists. The SASS solutions selected by the two methods are statistically similar, with exact agreement in about 75% of the cases. Chelton et al. (1989) conclude that the two methods disagree most often in regions of low wind speeds and/or highly variable wind directions (low directional steadiness). The directional discrepancies are generally small and random, however, so that spatially and temporally averaged wind fields constructed from the two datasets are in close agreement. The 14-day comparison thus suggests that a high degree of confidence can be placed in the accuracy of spatially and temporally averaged wind fields constructed from the full three months of SASS data.

In this paper, three one-month averages (corresponding approximately to July, August, and September 1978—see section 2) of global wind stress and related fields are computed from the SASS data on a 2.5° latitude–longitude grid. Descriptive analyses of these wind stress fields are presented in section 3. We believe the maps presented in this section to be the first globally accurate depictions of the vector and scalar magnitude averages, directional steadiness, and curl of monthly average wind stress over the world ocean. The SASS data are especially important for understanding wind forcing over the Southern Ocean and tropical oceans since climatological wind fields and operational analyses of near-surface winds from meteorological forecast centers are least reliable in these regions. The monthly-average SASS winds are compared with the Hellerman and Rosenstein (1983) climatological average wind stress in section 4. The beneficial impact that satellite scatterometry could have on ocean modeling is underscored in section 5 by a comparison of the global Sverdrup circulation computed from the SASS winds and the Hellerman and Rosenstein winds. Although the validity of the Sverdrup model on the short time scales addressable by the 3-month dataset is certainly arguable, the model intercomparison demonstrates the sensitivity of even simple ocean models to the differences between SASS and Hellerman and Rosenstein winds. Evidence of systematic errors in the Hellerman and Rosenstein wind stress values is presented in section 6. In section 7, the SASS data are compared with wind stress fields computed from contemporaneous operational surface wind analyses produced by the National Meteorological Center (NMC). The quality of the NMC winds has improved since the Seasat mission and a case might be made that other operational analyses were better than those of NMC. Nevertheless, the conclusions drawn from the comparison highlight limitations that may still exist in present-day operational wind analyses.

2. Data and methods

The primary dataset used in this study consists of 96 days of SASS vector winds supplied by R. Atlas at GSFC. The directional ambiguities in the raw SASS data had been objectively removed using the GSFC Laboratory for Atmospheric Sciences atmospheric general circulation model. The details of the ambiguity removal scheme are given by Atlas et al. (1987) and Chelton et al. (1989). The present study focuses on wind stress and wind stress curl fields estimated from the SASS vector wind data.

The wide swaths of the SASS allow winds over areas several hundred kilometers on a side to be measured nearly synoptically with high (~ 100 km) spatial resolution. Global coverage can be obtained only by using data acquired from several orbits. Because of the approximate 450 km nadir gap between the port and starboard swaths of a single orbit and additional spatial gaps between swaths from consecutive orbits, SASS measurements closely located in space may have been acquired from different orbits and thus may be widely separated in time. Since winds measured at a point can vary significantly over periods of a few hours, reconstruction of synoptic fields of surface winds on basin scales is not possible without extensive interpolation and extrapolation of the SASS measurements.

From the standpoint of short-term climate studies (time scales of months to years), many of the problems associated with deriving global *synoptic* wind fields from SASS data need not be addressed directly. Existing ocean and climate models parameterize the important short-scale, high-frequency interactions between the atmosphere and the ocean to allow study of the physics governing large-scale spatial and temporal variability. Spatial resolution of several degrees of latitude and longitude and temporal resolution of months to seasons are probably adequate for present global modeling capabilities.

The ability to resolve temporally averaged wind stress from discrete observations depends on the number and temporal distribution of the observations. From surface wind observations at islands in the tropical Pacific, Luther and Harrison (1984) conclude that approximately 30 observations are necessary for accurate estimates of monthly average winds over 2° × 10° areas. Halpern (1988) conducted a similar analysis of tropical Pacific winds measured from moored buoys along the equator and found that about ten observations are required to estimate monthly average surface winds at a
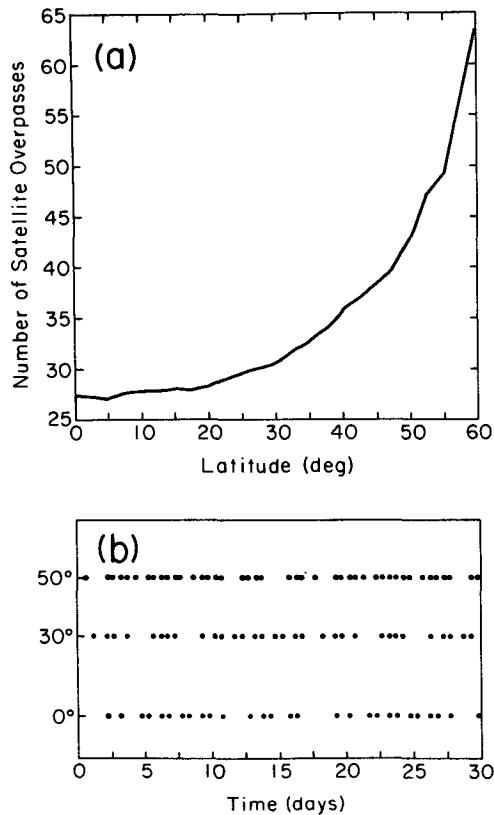
FIG. 1. (a) The average number of Seasat overpasses per 30-day period for a 2.5°-square region as a function of latitude for the period 7 July–15 August; there are typically several individual 100-km SASS estimates of vector wind in the 2.5° area during each overpass of the area; (b) the relative times of satellite overpasses during a typical 30-day period for 2.5°-square regions centered at latitudes of 0°, 30° and 50°.

point to an accuracy of 1 m s^{-1}. Both of these studies were limited to the tropics where the wind directions are very steady (see Fig. 4 below). The observational requirements are presumably greater at higher latitudes where the high frequency variability of wind speed and direction is generally more energetic.

The sampling distribution of SASS observations is summarized in Fig. 1. The number of SASS overpasses of a 2.5° latitude–longitude area during a 30-day period (Fig. 1a) increases from 27 at the equator to 35 at 40° of latitude and 49 at 55° of latitude; the increase with latitude is a consequence of the wide measurement swaths and convergence of satellite ground tracks at high latitudes. The relative times of the SASS overpasses can be seen from Fig. 1b to be relatively evenly distributed over the 30-day period. Additionally, there are typically several 100-km resolution SASS estimates of vector winds within a 2.5° area during each satellite overpass. The SASS data are thus more than adequate to meet the tropical sampling requirements deduced from island and buoy data. As shown in Fig. 10 of Chelton et al. (1989), the SASS sampling pattern yields

2.5° monthly average wind speed accuracies of better than 0.4 m s^{-1} at higher latitudes. The SASS data can therefore be used to construct global monthly average wind fields without the use of sophisticated interpolation and extrapolation schemes.

SASS observations of global near-surface winds span the period 7 July–10 October 1978. There are only two complete calendar months in these 96 days of data; both July and October were only partially sampled by Seasat. To maximize the use of the SASS data, the 96-day mission was divided into three periods of approximately one-month duration, as indicated in Table 1. The periods will be referred to here as July, August, and September, but it should be kept in mind that these monthly averages are actually shifted by six days from true July, August, and September.

The computational details of constructing wind stress and wind stress curl fields from the SASS data are summarized in the appendix. Briefly, wind stress was estimated from each SASS vector wind observation by bulk parameterization using the Large and Pond (1981) wind speed dependent drag coefficient. Initially, our interest was in the comparison between SASS winds and wind products from operational analyses (see section 7), which are archived on a 2.5° latitude–longitude grid. The individual SASS wind stress values were therefore vector averaged on the same 2.5° grid for the three monthly periods and full 96-day Seasat mission. A spatial low-pass filter was then applied to the vector average wind stress fields to remove residual sampling errors resulting from the irregular distribution of SASS observations over each averaging period due to the Seasat orbital characteristics. Scalar average wind stress magnitude and wind stress directional steadiness were gridded and then smoothed in the same manner. Wind stress curl fields were computed from the smoothed vector average wind stress fields using Stokes' Theorem, rather than centered first differences, to preserve spatial resolution.

3. Monthly average SASS wind stress fields

a. Middle and high latitudes

Global maps of vector average wind stress (in dyn cm^{-2}) and wind stress curl (in 10^{-9} dyn cm^{-3}) are shown for the three monthly periods and the full Seasat

TABLE 1. The calendar dates and Julian days of 1978 corresponding to the three monthly averages and full Seasat mission average examined in section 3.

Month	Calendar dates (1978)	Julian days (1978)
"July"	July 7–August 6	188–218
"August"	August 7–September 6	219–249
"September"	September 7–October 10	250–283
"July–September"	July 7–October 10	188–283

SASS Vector Average Wind Stress

July

1dyne/cm**2

September

1dyne/cm**2

August

July–September

1dyne/cm**2

mission in Figs. 2 and 5, respectively. Scalar average wind stress magnitude and directional steadiness are shown only for the full Seasat mission in Figs. 3 and 4. The major features known to exist in the wind stress field are clearly evident. Over most of the Northern Hemisphere, the monthly scalar average wind stress magnitude was 0.5–1.2 dyn cm^{-2}. Since the wind direction at a given location generally varies with time, the corresponding vector average wind stress was smaller (typically 0.3–0.7 dyn cm^{-2}). Directional steadiness ranged from highs of 0.8–0.9 in the northeast tradewinds of both the Pacific and Atlantic to lows of 0.2–0.4 near 40°N in the northwest regions of both basins. Directional steadiness was also low (about 0.4) in both the Pacific and Atlantic just north of the intertropical convergence zone (ITCZ, shown by the dashed lines in Fig. 4).

The weakest monthly average winds during the Seasat mission were in the horse latitudes (30°–40°) of both hemispheres. The vector average wind stress was less than 0.3 dyn cm^{-2} over much of the region, with directional steadiness generally about 0.4 in the Northern Hemisphere, decreasing to about 0.2 in the western North Pacific and western North Atlantic. Near the dateline in the horse latitudes of the South Pacific, the directional steadiness was only about 0.2 throughout the three-month period.

The wind stress in the northern hemispheres westerlies (40°–60°N) was moderate over most of the Seasat period with monthly vector averages generally less than 0.6 dyn cm^{-2} and typical directional steadiness about 0.4 (0.6 in the northeast Pacific). A rapid intensification of the eastward wind stress from 0.3 to 1.5 dyn cm^{-2} occurred during September in the high latitude North Atlantic. A general increase in the cyclonic wind stress from July to September is evident in the high-latitude northeast Pacific, indicating a seasonal fall transition from a mid-Pacific high pressure system centered near 40°N, 150°W to an Aleutian low pressure system centered near 50°N, 150°W. This resulted in a strong positive wind stress curl at about 50°N (Fig. 5) and a general southward shift of the region of subtropical negative wind stress curl (corresponding to a southward shift in the location of the mid-Pacific high) during September.

A noteworthy feature in the September wind stress field of the North Atlantic is the localized region of high wind stress (0.9 dyn cm^{-2} in the monthly average) centered at about 40°N, 55°W. This is a consequence of the intense QE-II storm which occurred in the western North Atlantic 9–12 September 1978 (Gyakum

1983). This storm was sampled during several orbits by SASS, but was poorly predicted by all operational forecast models in use at the time. Subsequent simulations have shown that the storm could have been accurately predicted had it been possible to assimilate SASS data into the models in near real time (e.g., Duffy and Atlas 1986). Though short-lived, the intensity of the wind stress in the QE-II storm affects the September monthly averages in several 2.5° grid squares in the western North Atlantic. The storm is also clearly evident in the September wind stress curl field as a localized region of very strong positive atmospheric vorticity off the east coast of North America. A similar localized region of strong positive vorticity can be seen in the July monthly average wind stress curl centered at about 20°N, 140°E in the western Pacific, associated with SASS sampling of Hurricane Trix (Hawkins and Black 1983). Other major storms during the Seasat period were not sampled often enough by SASS or did not persist long enough to have a significant effect on the monthly averages.

The broad-scale features characterizing the wind stress curl field over the subtropical and subpolar gyres of the Northern Hemisphere are clearly evident from Fig. 5. At middle latitudes, the wind stress curl was negative over both oceans with values of about -5×10^{-9} dyn cm^{-3}, reaching -10×10^{-9} dyn cm^{-3} in the eastern North Pacific. The wind stress curl was positive over the North Pacific subpolar gyre with values as high as about 5×10^{-9} dyn cm^{-3}. In the North Atlantic, positive wind stress curl values were restricted to the highest latitudes and generally were less than 2–3 ($\times 10^{-9}$) dyn cm^{-3}. An exception was the strong positive wind stress curl north of 55°N in September associated with the rapid intensification of the high latitude westerlies discussed previously.

The strongest winds during the Seasat period (corresponding to austral winter) were the high latitude westerlies of the Southern Hemisphere. The magnitude of monthly vector-average wind stress exceeded 1.5 dyn cm^{-2} and the scalar average wind stress magnitude exceeded 2.5 dyn cm^{-2} over much of the region between about 45° and 60°S. The region of largest vector-average wind stress shifted from the southeast Atlantic in July to the South Indian in August and spread from the South Indian to the South Pacific in September. The maximum monthly vector average stress was about 3.3 dyn cm^{-2} in July and August, decreasing to 2.7 dyn cm^{-2} in September. The wind stress directional steadiness south of 45°S in the South Atlantic and South Indian was moderately high (about 0.5–0.8)

FIG. 2. Monthly vector averages of the wind stress in dyn cm^{-2} for "July," "August" and "September" (see Table 1) and the full 96-day vector average for the Seasat mission ("July–September"). Wind stress was computed from the SASS vector winds and then averaged globally on a 2.5° grid and smoothed as described in the Appendix. Contours of the magnitude of the vector average wind stress are overlayed on the vectors with a contour interval of 0.3 dyn cm^{-2}. For graphical purposes, the 2.5° gridded vectors are plotted at intervals of 5° of latitude and 10° of longitude.
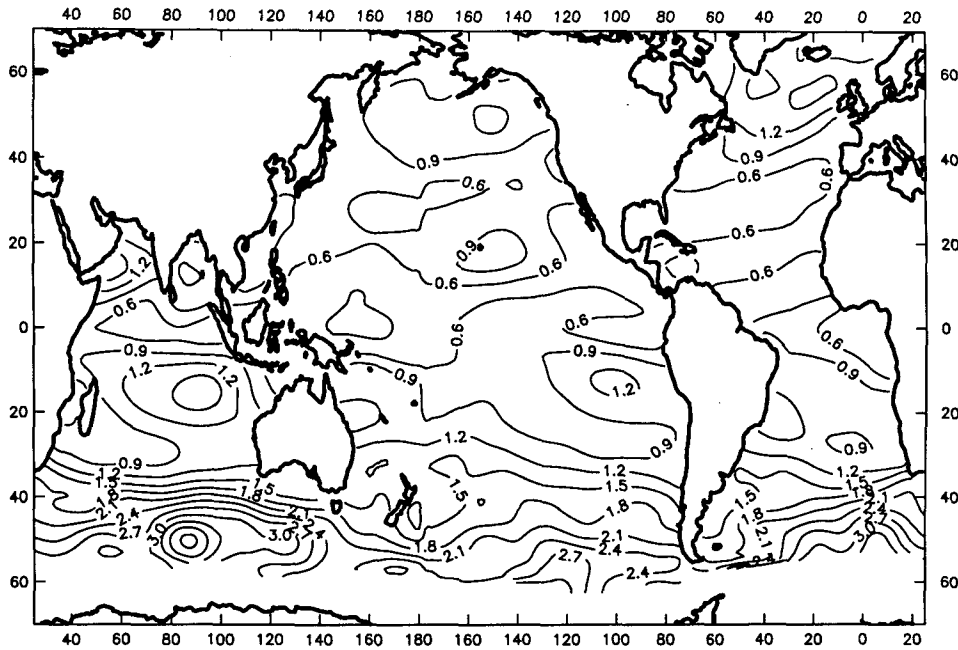
SASS Scalar Average Wind Stress Magnitude

FIG. 3. Wind stress magnitude in dyn cm^{-2}, scalar averaged over
the full Seasat mission. Contour interval is 0.3 dyn cm^{-2}.

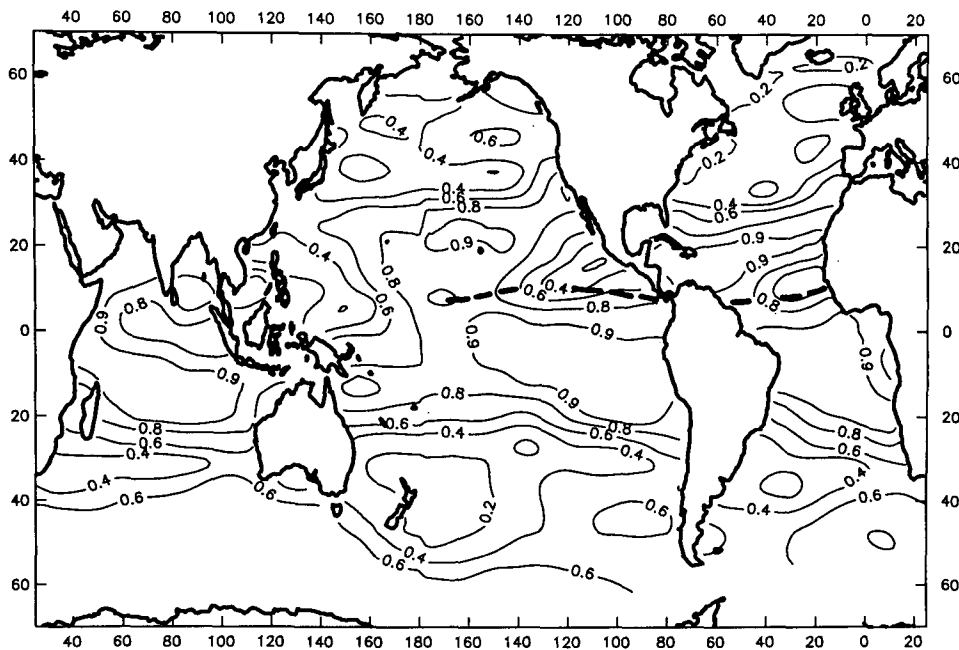## SASS Wind Stress Directional Steadiness

FIG. 4. The wind stress directional steadiness computed over the full Seasat mission (the magnitude of vector average wind stress divided by the scalar average wind stress magnitude). Contour interval is 0.2 with an additional contour for directional steadiness of 0.9. Dashed lines correspond to the location of the intertropical convergence zone (ITCZ) in the Pacific and Atlantic as determined from the location of maximum convergence in the SASS vector averaged wind fields (not shown).

throughout the Seasat mission. By comparison, the wind stress in the South Pacific sector varied dramatically over the period; the vector average wind stress in the westerlies was moderate during July (0.6–0.9 dyn cm^{-2}) with directional steadiness of about 0.4 in the western South Pacific, and very light (less than 0.3 dyn cm^{-2}) and variable (directional steadiness of only 0.2) just west of Drake Passage in the far eastern South Pacific. The July scalar average wind stress magnitude, however, exceeded 2.5 dyn cm^{-2} in the region west of Drake Passage. The low directional steadiness and the large difference between vector and scalar average wind stress imply that the region experienced repeated strong transient storms during July. The monthly vector average wind stress in the region west of Drake Passage reached a maximum of 2.4 dyn cm^{-2} in August with a directional steadiness of 0.6 and scalar average wind stress magnitude of 3 dyn cm^{-2}. By September, the eastward vector average wind stress had increased to 1.5–2.5 dyn cm^{-2} over most of the South Pacific and had become very steady (directional steadiness between 0.7 and 0.8) with scalar average wind stress magnitude of 2–3 dyn cm^{-2}.

The strong meridional shear in the zonal westerlies of the Southern Hemisphere (Fig. 2) results in a very strong wind stress curl (Fig. 5). The average curl over the full Seasat mission was positive nearly everywhere south of the tropics, except at the highest ice-free southern latitudes. In individual monthly averages, however, there is evidence of very large scale intense cyclonic and anticyclonic features at middle and high latitudes (especially in the South Pacific). The strongest wind stress curls reached exceptionally high values of 15–20 ($\times 10^{-9}$) dyn cm^{-3} on the northern side of the Southern Hemisphere westerlies. This positive wind stress curl, coupled with the zonal band of strong negative curl generally present at higher southern latitudes, indicates a jetlike characteristic of the wind stress in this region. The line of zero wind stress curl along the core of the jet had a northern-most location of about 45°S in the southeast Indian Ocean and a southern-most location poleward of 60°S in the South Pacific.
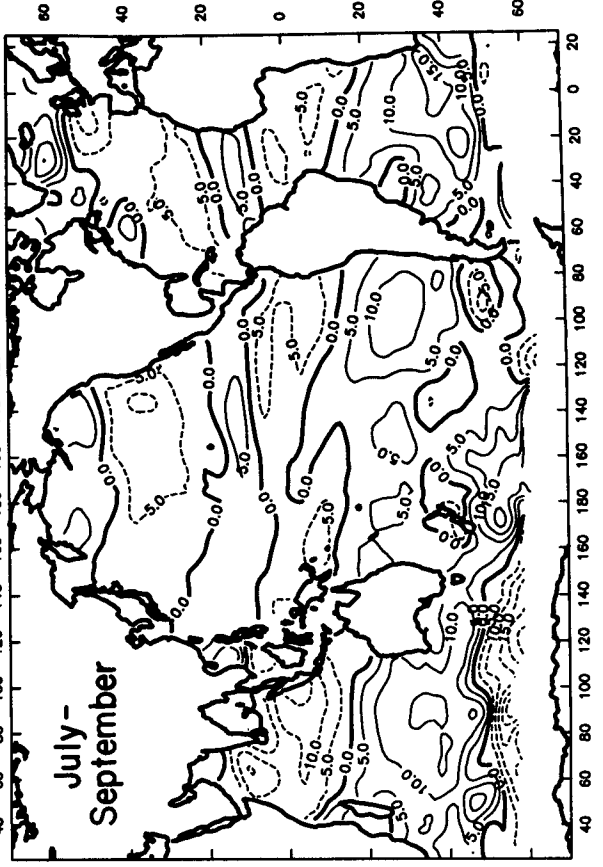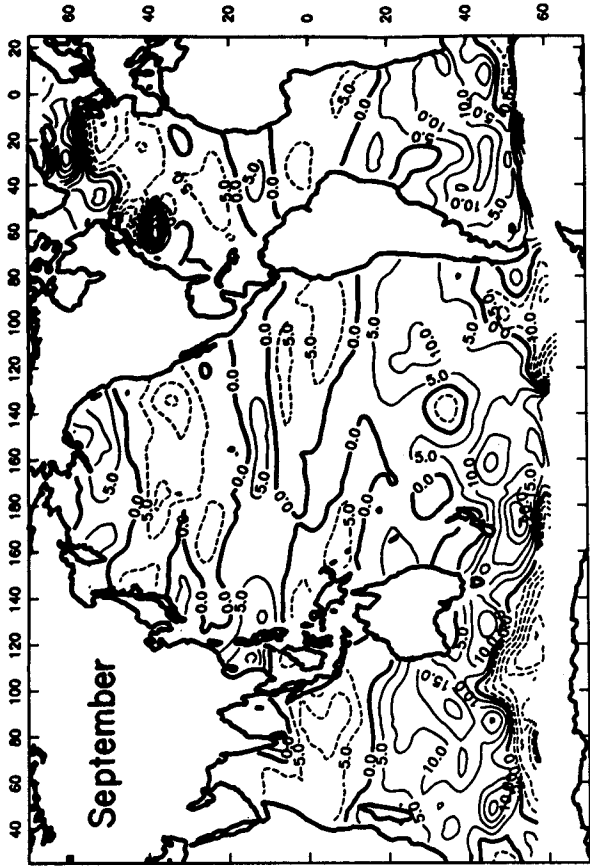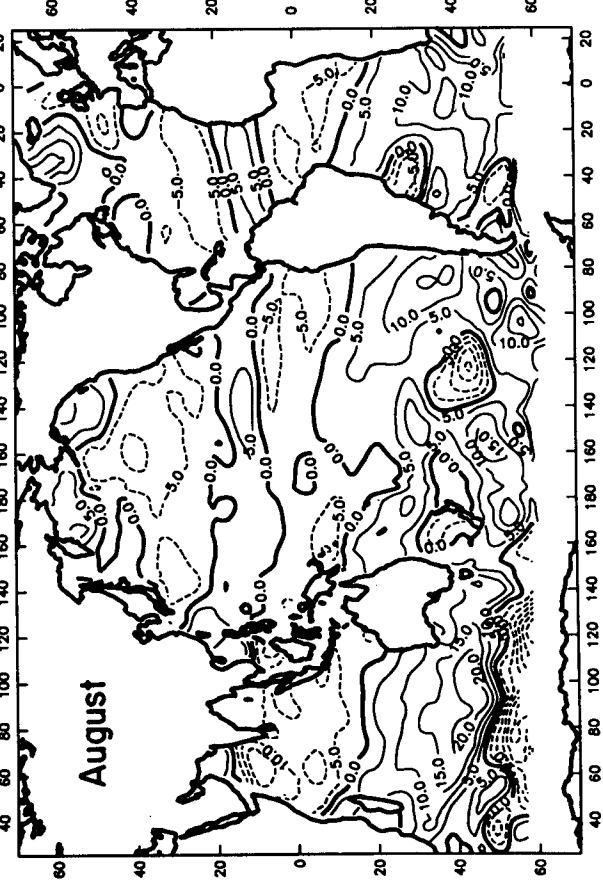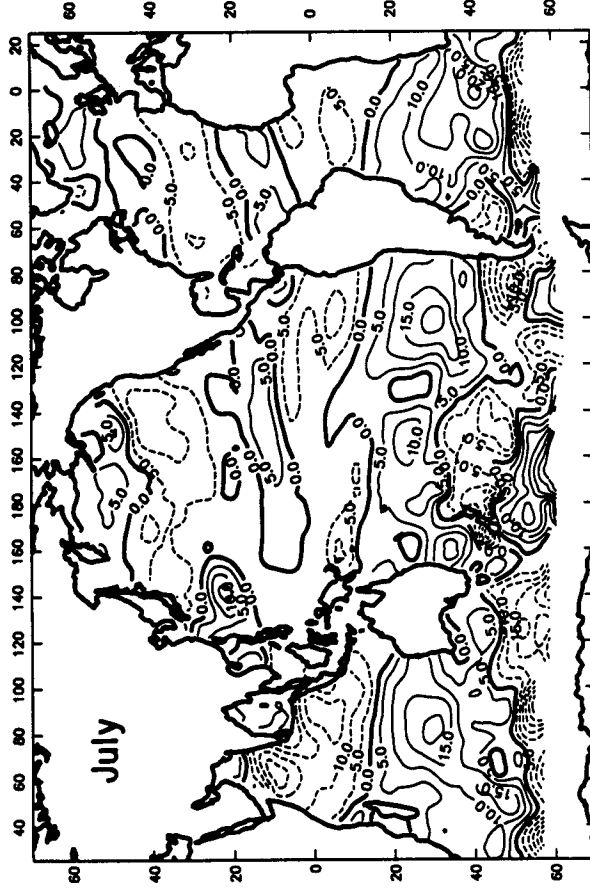
b. Tropics

Near-surface winds in the tropics are generally not well resolved in operational analyses (Reynolds et al. 1989; Trenberth et al. 1989). This geographical bias in the quality of the wind fields is not a problem with SASS, which measures the wind field with essentially uniform accuracy at all latitudes. Because numerous features present in the tropical SASS wind stress and wind stress curl fields are difficult to discern in the global maps of Figs. 2 and 5, expanded plots for the tropical Pacific, Atlantic and Indian Oceans are shown in Figs. 6–9 with smaller contour intervals and no decimation of the plotted stress vectors. These tropical maps have also been smoothed only half as much as the global maps of Figs. 2 and 5 (see Appendix).

The wind stress was predominantly westward everywhere between 30°S and 30°N, except in the northern Indian Ocean where the wind stress field was dominated by the seasonal southwest monsoon. The vector average wind stress in the southeast tradewinds was as strong as 1.2 dyn cm^{-2} in the Atlantic and Pacific and 1.5–2.1 dyn cm^{-2} in the Indian Ocean. The tradewinds were remarkably steady (wind stress directional steadiness of 0.8–0.9, see Fig. 4) everywhere except in the western Pacific and just north of the ITCZ in the eastern Pacific where the directional steadiness was as low as 0.3 in both regions, and just north of the ITCZ of the eastern Atlantic where the steadiness was as low as 0.4. The low directional steadiness north of the ITCZ evidently results from fluctuations in the directions of the very light winds in these regions.

An interesting feature clearly present in Fig. 6 is the narrow band of locally high northward wind stress (greater than 0.6 dyn cm^{-2}) just north of the equator in the eastern tropical Pacific from the South American continent to about 120°W. Immediately to the south is a narrow zonal band of relatively weak wind stress (less than 0.4 dyn cm^{-2}). This pair of features has previously been described by Chelton et al. (1981) in terms of scalar average wind speed measured by the Seasat altimeter. Similar bands of light wind stress just south of the equator and strong northward wind stress just north of the equator are also evident in the eastern tropical Atlantic (see Fig. 8). These narrow bands of strong northward winds are not evident in operational wind analyses (see section 7). They have been observed in the Pacific from low-level cloud motion vectors (Sadler and Kilonsky 1981), and are present in the pseudostress wind analyses generated at Florida State University (FSU) by subjective analysis of direct wind observations from ships of opportunity (O'Brien and Goldenberg 1982; Legler and O'Brien 1984).

Wallace et al. (1989) and Hayes et al. (1989) have recently suggested that the parallel zonal bands of weak and strong southerly winds, and the associated zonal band of divergence along the equator, are the result of meridional pressure and sea surface temperature gradients in the eastern tropical Pacific. As northward moving air parcels driven by horizontal pressure gradients cross from the tongue of cold, upwelled water along the equator to warmer water to the north, the atmospheric boundary layer undergoes a transition from a stable to an unstable regime. The result is an enhanced downward flux of northward momentum from buoyancy-driven turbulence, and hence an increase in surface wind stress. Wallace et al. (1989) argue that these bands of strong meridional winds may be responsible for the northward displacement of the ITCZ (see dashed lines in Fig. 4). During episodes of anomalous warm water along the equator (e.g., during El Niño events), the zonal band of strong southerly winds may weaken or shift southward and the ITCZ may become more amorphous or shift southward.

SASS Wind Stress Curl

July

September

August

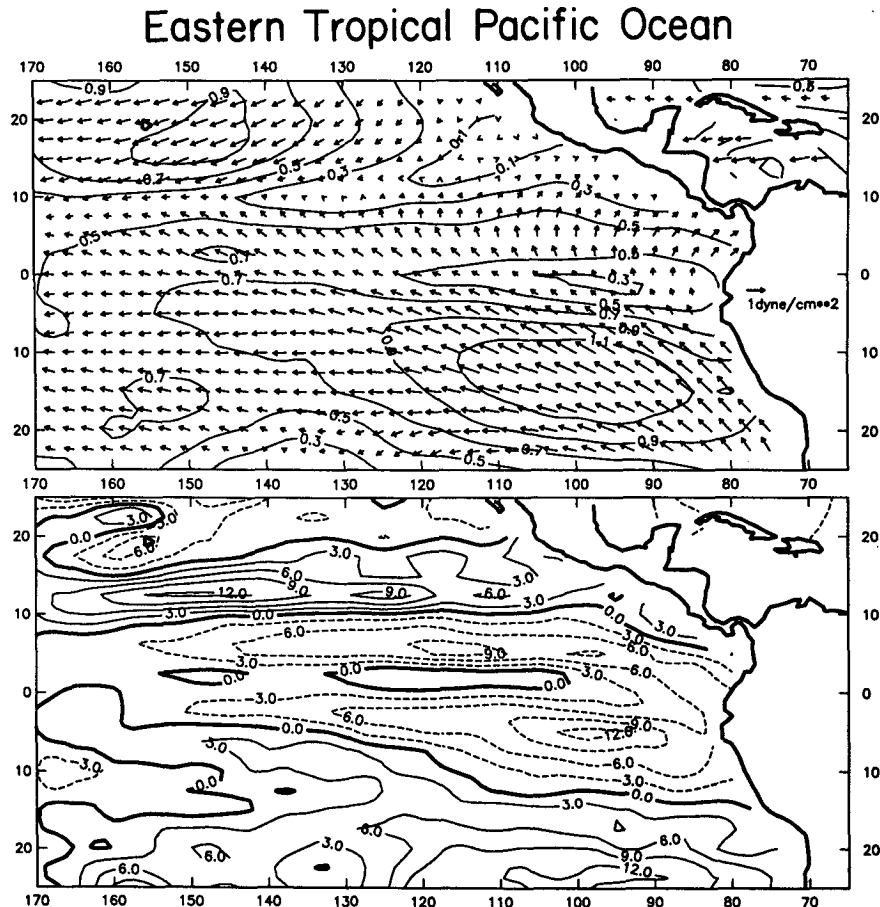July–
September

Eastern Tropical Pacific Ocean

FIG. 6. Expanded plots of the vector average wind stress and wind stress curl fields for the full Seasat mission for the eastern tropical Pacific. The 2.5° averaged data were smoothed half as much as the global maps of Figs. 2 and 5 (see Appendix) and the vectors are plotted for each 2.5° region.

On shorter time scales of weeks to months, Hayes et al. (1989) find a correlation between wind divergence and the meridional gradient of sea surface temperature in the eastern tropical Pacific. They suggest that perturbations in the zonal jet of meridional winds are coupled to variations in the meridional gradient of sea surface temperature associated with instability waves in the ocean. The physical coupling is the same as that suggested on longer time scales by Wallace et al. (1989), namely destabilization of the atmospheric boundary layer as air parcels move northward from the cold, upwelled equatorial water to warmer water to the north.

The wind stress fields in the tropical Pacific and Atlantic result in zonal bands of wind stress curl which force the complex system of currents and countercurrents in the equatorial regions. North of the ITCZ in both the Atlantic and Pacific, there was a narrow (about

10° of latitude) zonal band of positive wind stress curl as strong as 8×10^{-9} dyn cm^{-3} in the Atlantic (Fig. 8) and 9–12 ($\times 10^{-9}$) dyn cm^{-3} in the Pacific (Fig. 6). There were two parallel zonal bands of strong negative wind stress curl (as large as -6 to -9 ($\times 10^{-9}$) dyn cm^{-3}) straddling the equator in the eastern tropical Atlantic and Pacific. The narrow zonal band of zero wind stress curl along the equator in the eastern tropical Pacific between 100° and 160°W is not resolved in either the FSU pseudostress fields for the period July–October 1978 or the Hellerman and Rosenstein (1983) climatological wind stress fields. Though not as well defined as in the Pacific, a similar zonal band of weak wind stress curl is present along the equator in the tropical Atlantic SASS data.

In the western tropical Pacific (Fig. 7), the dominant Northern Hemisphere feature is a large region of very

FIG. 5. Monthly averages and the average over the full Seasat mission of the wind stress curl in 10^{-9} dyn cm^{-3} computed from the smoothed wind stress fields as described in the Appendix. Contour interval is 5×10^{-9} dyn cm^{-3} with the zero contour plotted as a heavy line and negative contours plotted as dashed lines.
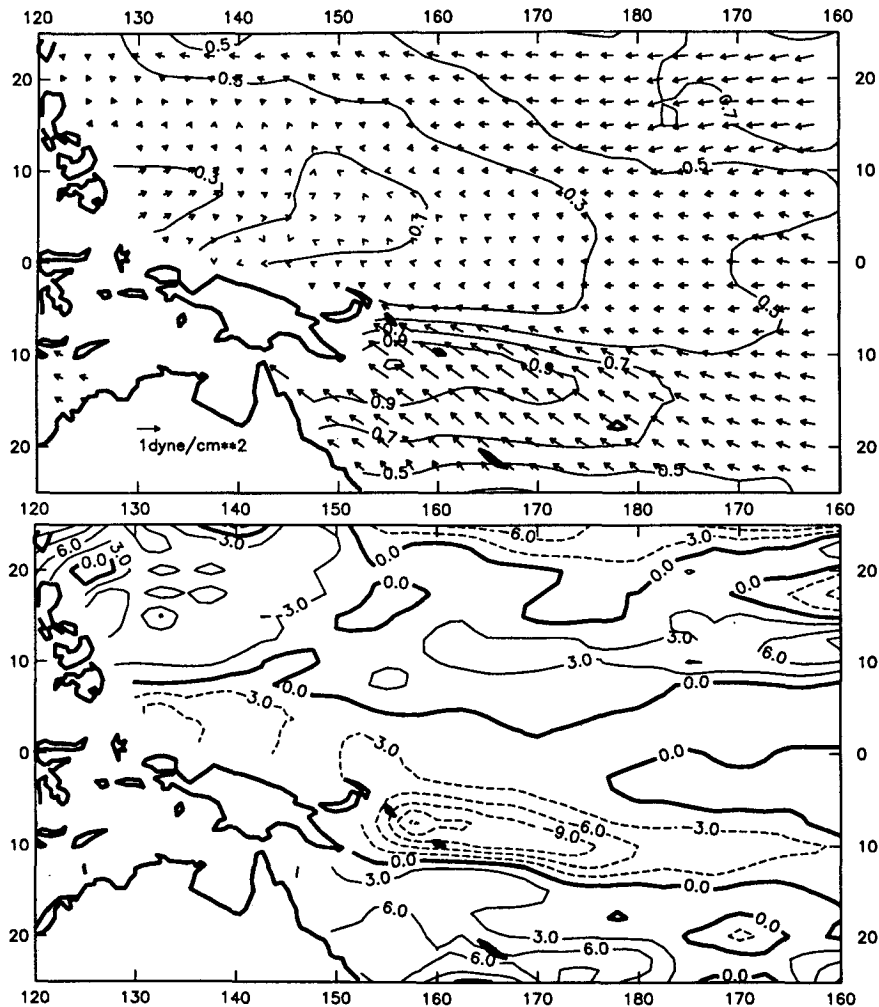
Western Tropical Pacific Ocean

FIG. 7. As in Fig. 6, except for the western tropical Pacific.

low wind stress (less than 0.3 dyn cm^{-2}) west of 170°E. The minimum vector average wind stress is located near 5°N, 150°E. Farther west, increasing westerly winds are apparent north of the equator between 2° and 12°N. South of the equator, the southeast trade-winds rapidly increase in strength and turn northward to feed the low stress region of surface convergence. A zonal tongue of strongly negative wind stress curl (about −9 × 10^{-9} dyn cm^{-3}) marks the southern boundary of the convective zone and coincides with the South Pacific convergence zone along 10°S.

In the northwest Indian Ocean (Fig. 9), the vector average northeastward monsoon wind stress was as high as 2.5 dyn cm^{-2} with directional steadiness greater than 0.9 during July and August. The winds in this region decreased to less than 0.5 dyn cm^{-2} and became more variable (steadiness between 0.7 and 0.9) in September in association with the spindown of the monsoon. The

wind stress curl patterns in the northwest Indian Ocean also changed dramatically during the Seasat mission. The negative wind stress curl resulting from strong horizontal gradients in the monsoon winds decreased from a maximum of −27 × 10^{-9} dyn cm^{-3} in July to −15 × 10^{-9} dyn cm^{-3} in August and only −6 × 10^{-9} dyn cm^{-3} in September when the monsoon winds had diminished. A decrease from −21 × 10^{-9} dyn cm^{-3} to −15 × 10^{-9} dyn cm^{-3} is also evident in the wind stress curl patterns over the eastern Indian Ocean near the equator, evidently also associated with the spindown of the monsoon winds.

4. Comparisons with climatological data

The wind stress fields most commonly used to date to force recent models of ocean circulation are climatological monthly averages such as those compiled
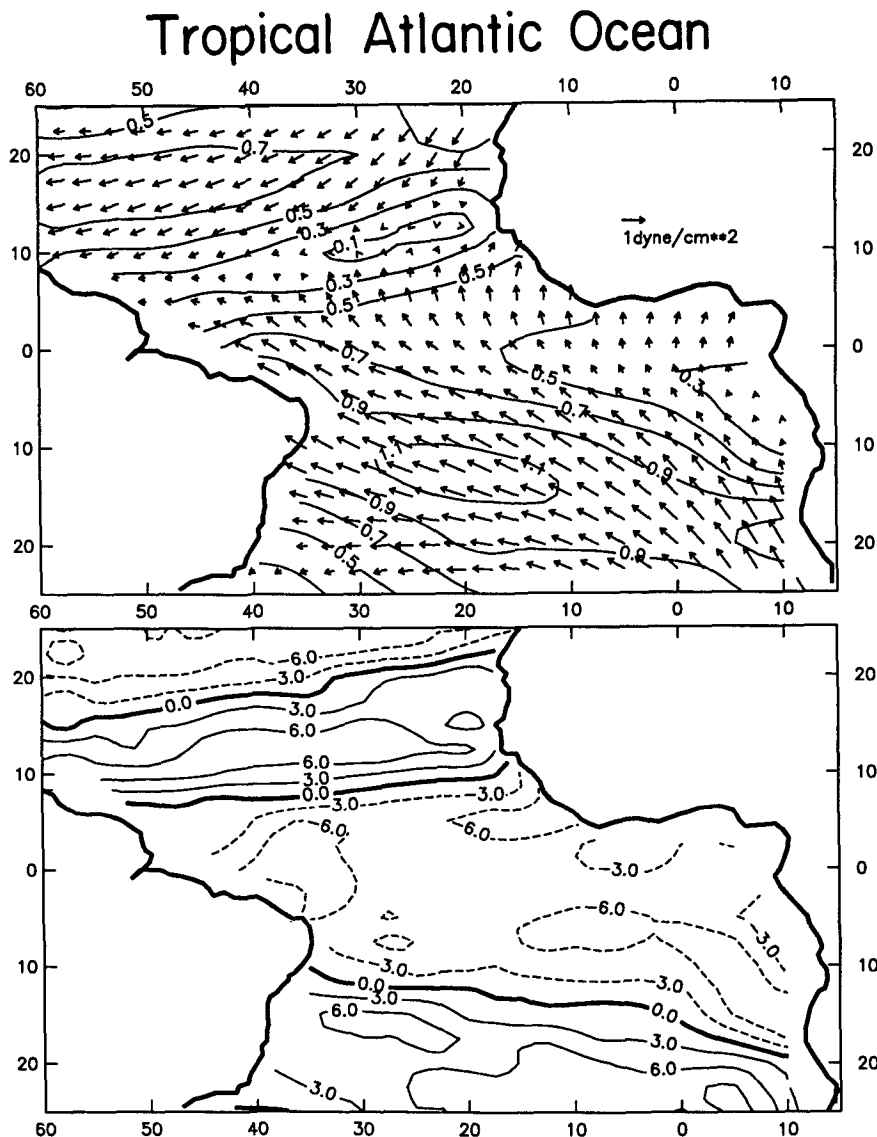
Tropical Atlantic Ocean

FIG. 8. As in Fig. 6, except for the tropical Atlantic.

by Hellerman and Rosenstein (1983, hereafter referred to as HR) computed from direct observations of vector winds from ships of opportunity. A new surface wind stress climatology computed from operational analyses of winds at 1000 mb by the European Centre for Medium-range Weather Forecasting (ECMWF) has very recently been made available by Trenberth et al. (1989). Evaluation of this ECMWF climatology is beyond the scope of this study. In this section, the wind stress fields computed from the SASS data are compared with the HR climatological averages for the months of the Seasat mission. These comparisons must be interpreted with some degree of caution since discrepancies are not necessarily indicative of errors in either dataset. Some differences are to be expected due to deviations of the 1978 wind field from the clima-

tological normal. As will become apparent from the comparisons, however, the quality of the HR winds is suspect in some regions.

The HR wind stress climatology was constructed from 100 years of ship observations of vector winds, supplemented by U.S. Navy wind-rose data in the data-sparse high latitude regions of both hemispheres. The HR data are available globally as 2° latitude–longitude averages, with some degree of smoothing applied in data sparse regions. For comparison with the SASS wind stress fields in section 3, the HR data were interpolated to the SASS 2.5° grid using two-dimensional cubic spline interpolation. The HR climatological averages are for true calendar months. The SASS averages analyzed in section 3 were for the monthly periods given in Table 1, which are shifted by 6 days from true

Tropical Indian Ocean
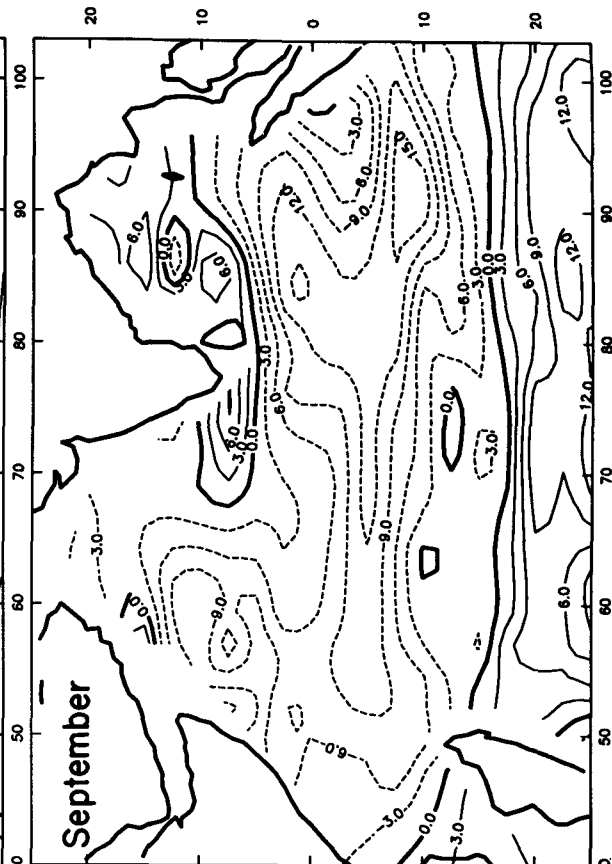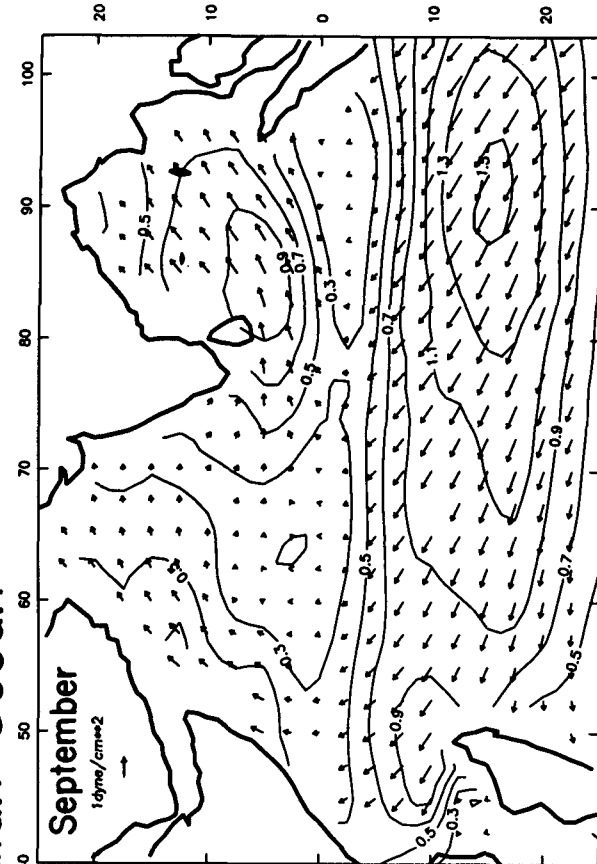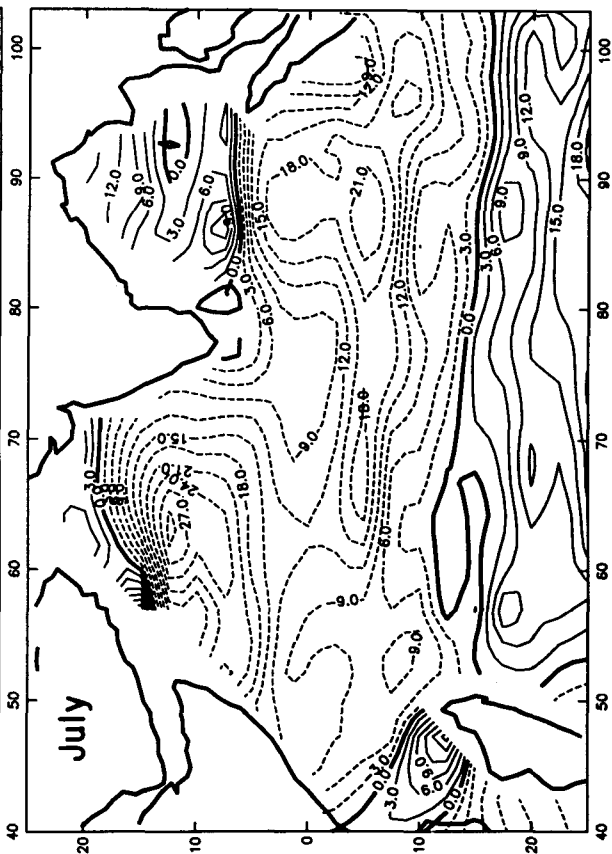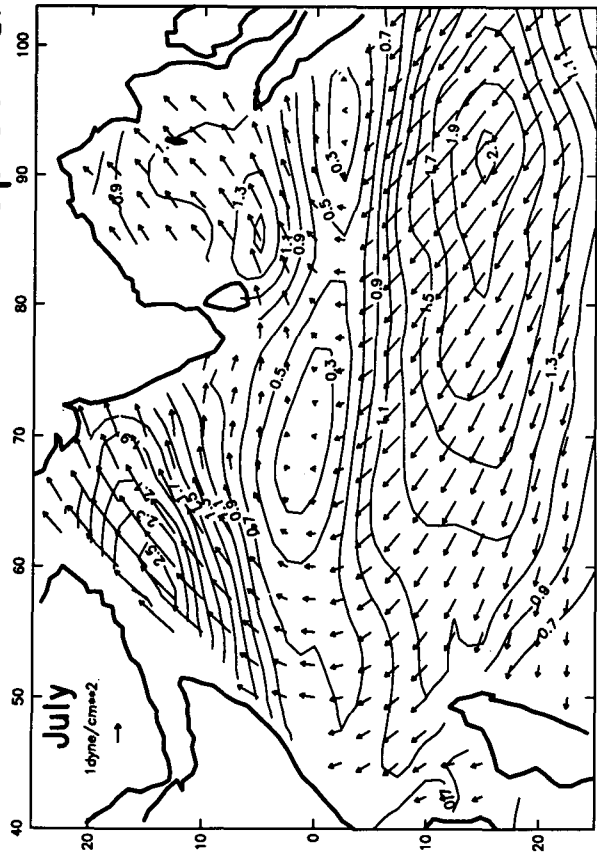
calendar months. To avoid potential confusion between interannual variability and different averaging periods, smoothed SASS monthly average wind stress fields were recomputed for the two calendar months completely sampled by SASS (August and September). The HR monthly wind stress fields exhibited noisy characteristics in many areas of the Southern Hemisphere, so they were smoothed in the same manner as the SASS data (see Appendix).

The August and September monthly averages of HR wind stress (not shown) were subtracted from the calendar monthly averages of SASS wind stress to obtain the vector difference maps shown in Fig. 10. Although not obvious from these monthly averages, there is an apparent small multiplicative scaling error in the HR wind stress values that is discussed at length in section 6. Otherwise, the SASS and HR vector average wind stress fields generally agree to within 0.3 dyn cm^{-2} north of 35°S. This result is somewhat surprising, indicating that the winds during the Seasat mission apparently did not generally deviate substantially from the climatological norm over much of the world ocean.

There are several notable exceptions of climatologically abnormal atmospheric conditions. The presence of the QE-II storm in the September SASS data is evident as the localized region of large wind stress difference (as much as 1.2 dyn cm^{-2}) in the western North Atlantic. In addition, the strong winds noted previously from the September SASS data in the high latitude North Atlantic (north of 55°N) can be seen from the difference map to be stronger than the HR climatological average by 0.6-0.9 dyn cm^{-2}. The region of 0.6 dyn cm^{-2} cyclonic differences off the west coast of North America in September suggests that the fall deepening of the Aleutian low may have been stronger than normal (perhaps occurring earlier than the seasonal norm) during the Seasat mission. In the northwest Indian Ocean, the SASS wind stress was consistently weaker than the HR wind stress. These monsoon wind stress differences were as large as 0.6 dyn cm^{-2} in August, decreasing to 0.3 dyn cm^{-2} in September (except for a small region centered at 10°N, 55°E). The SASS average wind stress over just the last three weeks of July (not shown) was 1.2 dyn cm^{-2} weaker than the HR July monthly average wind stress in the northwest Indian Ocean. This may be an indication that the monsoon winds were abnormally weak during July and August of 1978. Alternatively, the HR climatological average monsoon wind stress may be systematically too high, possibly due to sampling biases.

The largest differences between the SASS and HR wind stress fields are at the high latitudes of the Southern Hemisphere (south of 35°S). The SASS eastward wind stress was stronger than the HR climatological average by more than 0.9 dyn cm^{-2} across nearly all

of the Southern Ocean, with differences as large as 2 dyn cm^{-2} in some regions. In a zonal band between about 25° and 40°S across most of the South Indian Ocean, the SASS wind stress was persistently weaker than the HR climatological average eastward wind stress by 0.6–1.2 dyn cm^{-2}. The SASS winds were similarly weaker than the HR westerly winds between 35° and 45°S in the South Atlantic.

Since available climatological estimates of the near-surface meteorology at high southern latitudes are all suspect, it is difficult to judge how much of the large differences between SASS and HR wind stress over the Southern Ocean is due to abnormal meteorological conditions during the period of the Seasat mission. The SASS July wind field (Fig. 2) indicates the presence of a strong blocking high near 55°S, 175°W. In August, this anticyclone near the dateline had moved north to about 40°S. This region east and south of New Zealand is climatologically the primary location of blocking in the Southern Hemisphere (Trenberth and Mo 1985).

Based on monthly-average Australian Bureau of Meteorology sea level pressure analyses for July–September 1978 (Fig. 11), the New Zealand blocking high was more than 10 mb more intense than normal centered near 70°S, 160°W during July. At the same time, there was a negative pressure anomaly of more than a −10 mb centered near 45°S, 100°W. These pressure anomalies imply that the westerlies in the South Pacific were anomalously weak and the storm track was displaced southward during July 1978. The pressure was within about 5 mb of normal in the South Atlantic and South Indian Oceans during July and throughout the Southern Ocean during August and September. From these sea level pressure analyses, the meteorology thus appears to have been only slightly anomalous during the August and September periods in Fig. 10. In the three-month average, there were pressure anomalies of approximately −5 mb and 5 mb in the eastern and western South Pacific, respectively, but pressure was within 5 mb of normal elsewhere. Thus, during the three-month averaging period used in section 5 to compute the Sverdrup circulation, the storm track (approximately coincident with the line of zero wind stress curl) appears to have been displaced southward from normal in the South Pacific due to somewhat anomalous meteorological conditions. Elsewhere, the storm track appears to have been near normal.

Anomalous meteorological conditions may therefore explain some of the discrepancies between HR and SASS winds in the South Pacific. The nearly normal pressure patterns in the South Atlantic and South Indian Ocean suggest that the differences between HR and SASS wind stress in these two basins are more likely due to systematic biases in the HR data. Such systematic errors would not be surprising since the high

FIG. 9. As in Fig. 6, except for the tropical Indian Ocean for the months of July and September, rather than the full Seasat Mission.
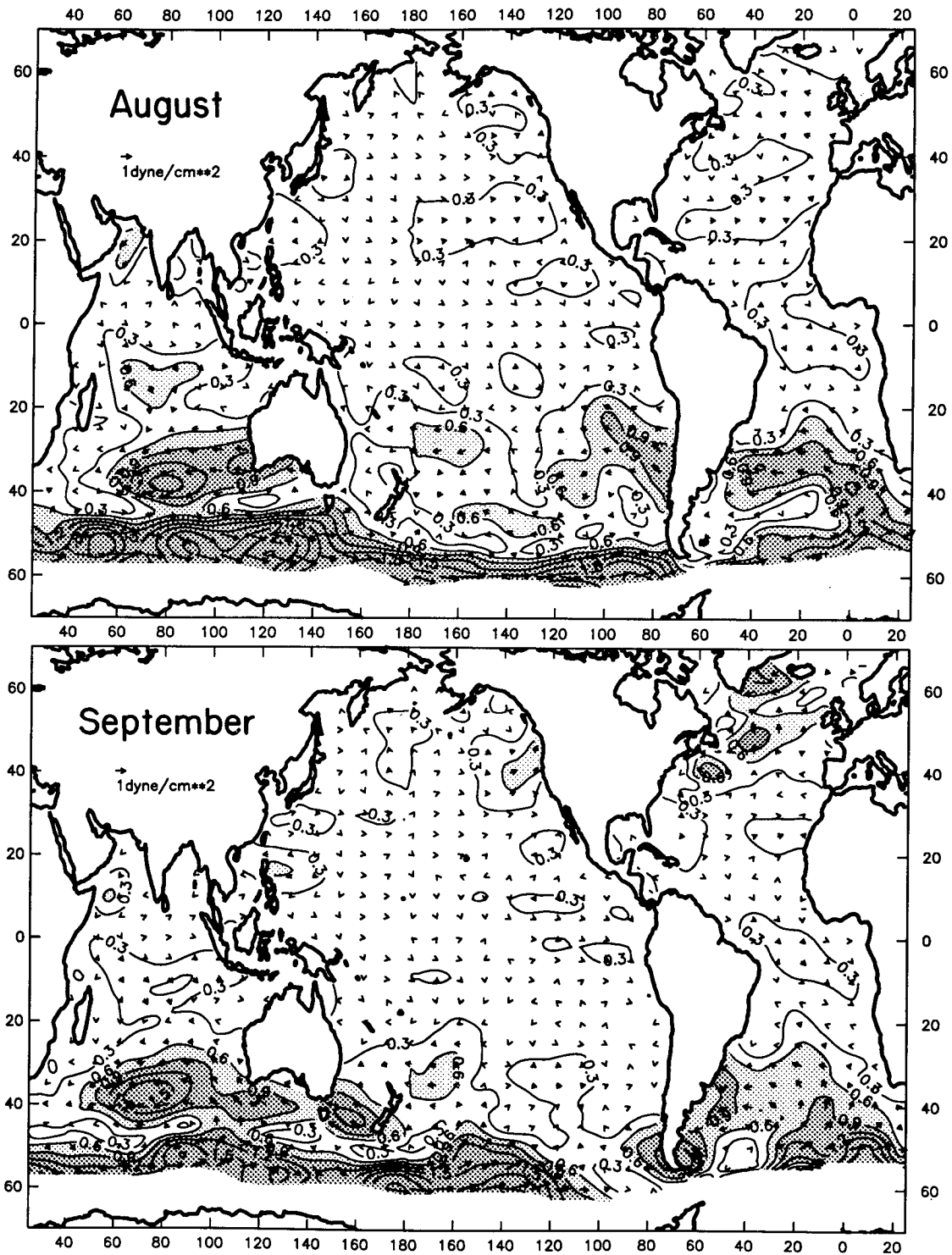
SASS minus HR Wind Stress

FIG. 10. Differences between vector average wind stress computed for the actual calendar months of August and September from SASS data and the Hellerman and Rosenstein (1983) (HR) climatological averages. The smoothing applied to the SASS data as described in the Appendix was also applied to the HR data. The plots are for the differences SASS minus HR. Contours of the magnitude of the differences (SASS minus HR, with contour interval of 0.3 dyn cm^{-2}) are overlayed on the vector differences (decimated for plotting as in Fig. 2). Areas with differences greater than 0.6 dyn cm^{-2} are lightly stippled and differences greater than 0.9 dyn cm^{-2} are heavily stippled.
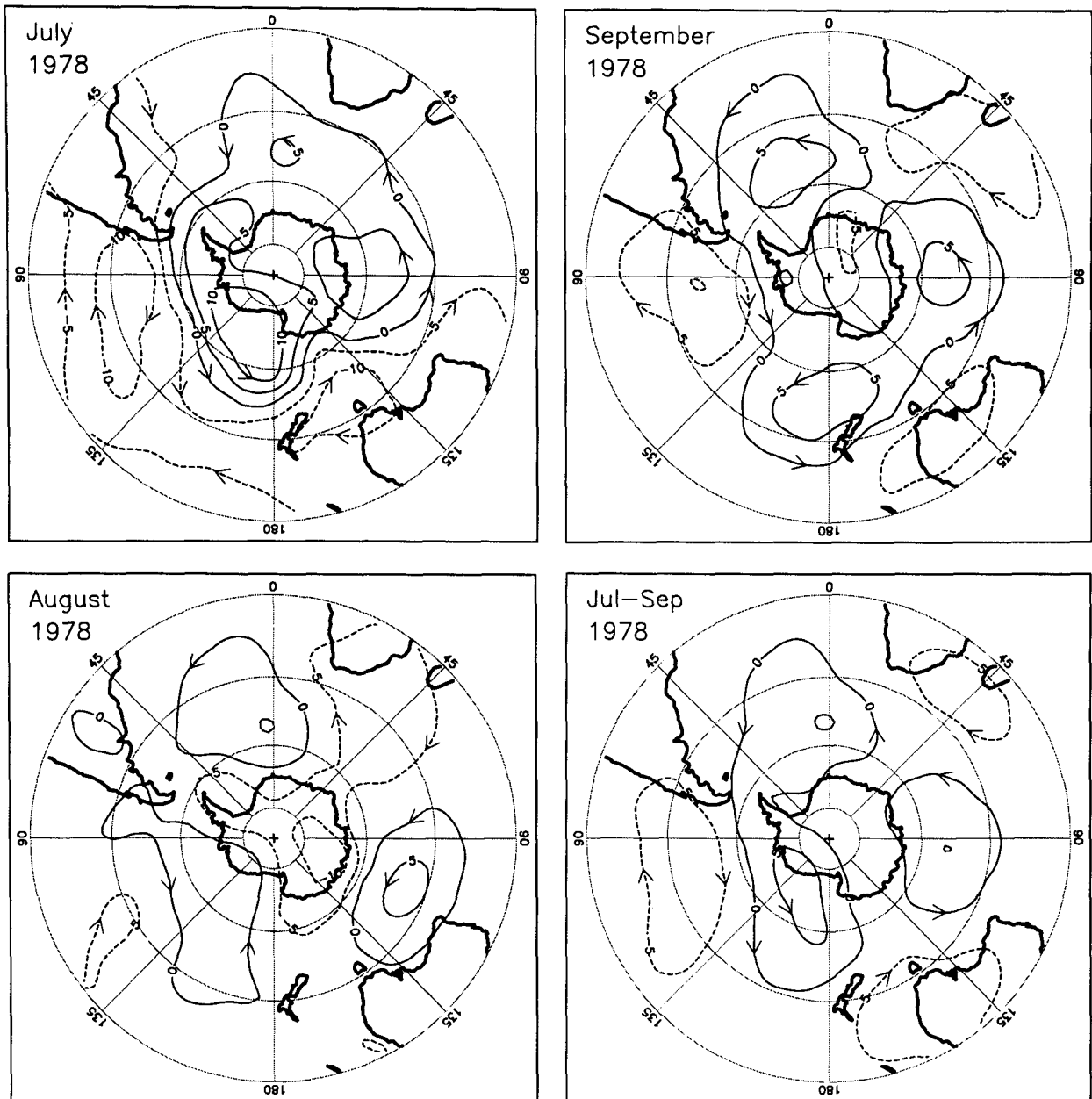
FIG. 11. Anomalous monthly-average sea level pressure analyses from the Australian Bureau of Meteorology for July, August and September 1978 and the three-month average for the period July–October 1978. Anomalies are defined here to be the deviations of the sea level pressure analyses from the long-term averages computed from the Australian Bureau of Meteorology data for the 9-year period 1975–1983. Contour interval is 5 mb and negative contours are shown as dashed lines. Latitude lines are plotted at 20° intervals. Arrows indicate the direction of anomalous geostrophic winds.

southern latitudes have the smallest numbers of historical ship observations, and hence the highest uncertainties, in the HR climatological averages. Moreover, the Seasat mission coincides with the austral winter, which is the period with the smallest number (of an already small number) of historical ship observations over the 100-year record. HR indicate that their wind stress estimates at high latitudes are likely biased low during the wintertime and quote a standard error of 0.5 dyn cm^{-2} over the Southern Ocean. The comparison in Fig. 10 suggests that the errors in the HR wind stress south of 45°S are likely to be considerably larger.

5. Sverdrup circulation

The results of section 4 indicate that the differences between monthly average SASS and HR wind stress

are consistent over much of the world ocean with what would be expected from year-to-year variability of the wind field. The discrepancies that exist north of 35°S can be associated with known or plausible anomalous events in the wind field during the Seasat period. The differences between SASS and HR data at high southern latitudes, however, are exceptionally large. These discrepancies are due to a combination of anomalous winds during the Seasat mission (especially the South Pacific sector) and sampling errors (all three basins) in the HR data. The contribution due to sampling errors could lead to large errors in model simulations of ocean circulation forced by HR winds. Model sensitivity to the differences between the SASS and HR winds is examined in this section using estimates of the global Sverdrup circulation computed from SASS and HR data. This simple model of ocean circulation has proven successful at reproducing many of the general features of large-scale ocean circulation. We emphasize that the purpose of these calculations is not to demonstrate the validity of the Sverdrup model on the short time scales addressable with the 3-month SASS dataset. Rather, the intent is to demonstrate the sensitivity of even this simple model to the differences between SASS and HR winds.

The Sverdrup circulation was computed in the usual way (e.g., Pedlosky 1987) from the linearized, time-independent, vertically-integrated momentum and continuity equations. Let x and y be the Cartesian coordinates along zonal and meridional axes, respectively, with positive directions eastward and northward. The streamfunction ψ (in $m^3 \ s^{-1}$) of the volume transport of the Sverdrup circulation is related to the wind stress τ by

$$\psi(x) = \int_{x_0}^{x} \frac{1}{\rho\beta} (\nabla_H \times \tau) dx' + \psi(x_0), \qquad (1)$$

where ρ is the water density, $\beta = df/dy$ is the latitudinal variation in the Coriolis parameter $f = 2\Omega \sin\theta$ for earth rotation rate Ω and latitude θ, and $\nabla_H = x\partial/\partial x + y\partial/\partial y$ for unit vectors x and y along the x and y axes. The streamfunction is related to the vertical integrals of the two velocity components by $U = -\partial\psi/\partial y$, $V = \partial\psi/\partial x$. The total northward volume transport in $m^3 \ s^{-1}$ across a zonal line between points x_1 and x_2 is thus

$$\int_{x_1}^{x_2} Vdx = \psi(x_2) - \psi(x_1). \qquad (2a)$$

Similarly, the total eastward volume transport across a meridional line between any two points y_1 and y_2 is

$$\int_{y_1}^{y_2} Udy = \psi(y_1) - \psi(y_2). \qquad (2b)$$

Traditionally, the Sverdrup volume transport streamfunction is computed from (1) by integrating

the curl of the wind stress westward along latitude lines from an eastern boundary at x_0 (which can vary latitudinally). The boundary condition of no perpendicular flow at a rigid boundary requires ψ to be constant along the eastern boundary $x_0(y)$; the initial value $\psi(x_0)$ is set to zero by convention. In both the Atlantic and the Pacific oceans, a continuous eastern boundary exists from the northernmost latitudes of each basin to the Southern Ocean. In the Atlantic, the southern limit of the eastern boundary is the southern tip of South Africa (Cape of Good Hope) at about 35°S; in the Pacific, it is the southern tip of South America (Cape Horn) at about 55°S. In the Indian Ocean, a continuous eastern boundary exists from the northernmost latitude to the northern side of the Indonesian passageway between the Pacific and Indian oceans at about 10°S, 125°E.

In the Northern Hemisphere, there are no significant land masses to interrupt the zonal integration in (1) within each ocean basin, so the Sverdrup circulation can be computed in a straightforward manner at all latitudes. In the Southern Hemisphere, however, New Zealand and Australia interrupt the integration. Since these both represent rigid boundaries, ψ must be constant (but not necessarily zero as along the eastern boundaries) around the boundary of each "island." The westward integration of $\nabla_H \times \tau$ must be stopped at the eastern sides of New Zealand and Australia. The integration can then be restarted on the western sides using an initial value of ψ computed by "the island rule" first developed by J. S. Godfrey (personal communication 1987), which relates the streamfunction at the island to the integral of the wind stress around a closed path enclosing the island (see deSzoeke 1987; Godfrey 1989). The four sides of the closed path of integration are defined by the eastern boundary of the basin, the western boundary of the island, and zonal lines from the northern and southern limits of the island to the eastern boundary of the basin (see Fig. 15 of deSzoeke 1987).

The island rule is easily derived by integrating the vertically integrated momentum equation along the closed path. In vector form,

$$\oint f z \times V \cdot ds = -\oint \frac{\nabla_H P}{\rho} \cdot ds + \oint \frac{\tau}{\rho} \cdot ds, \qquad (3)$$

where z is a unit vector along the vertical axis, ds is a unit vector parallel to the path of integration, P is the vertically integrated pressure and V is the vertically integrated vector velocity. The first integral on the right hand side vanishes around the closed integration path. Using (2a) and (2b), the left-hand side becomes

$$\oint f z \times V \cdot ds = (f_S - f_N)[\psi_I - \psi(x_0)], \qquad (4)$$

where f_S and f_N are the values of the Coriolis parameter at the southern and northern limits of the island and

ψ_I is the island value of the streamfunction. Since $\psi(x_0)$ = 0 along the eastern boundary segment of the integration path, (3) and (4) reduce to

$$\psi_I = \frac{1}{\rho(f_S - f_N)} \oint \tau \cdot d\mathbf{s}. \qquad (5)$$

The Sverdrup circulation in the Tasman Sea between New Zealand and Australia is computed by integrating (1) from the west coast of New Zealand using the initial value $\psi(x_0) = \psi_I$ determined from (5) for New Zealand. Similarly, the Sverdrup circulation south of 10°S in the Indian Ocean is computed by integrating (1) from the west coast of Australia using the value of $\psi(x_0)$ = ψ_I determined from (5) for Australia. The boundary of Australia was defined so as to include New Guinea since the water depth between Australia and New Guinea is everywhere less than 200 m. The values of ψ_I obtained in this study using the 96-day average SASS and both the 3-month and 12-month average HR winds are listed in Table 2. Note that the values based on the 12-month average HR wind stress field differ by 1–2 Sv (1 Sv $\equiv 10^6$ m^3 s^{-1}) from the corresponding values obtained by deSzoeke (1987) and Godfrey (1989). These small differences are likely due to the smoothing applied here to the HR winds (see Appendix) and slightly different definitions of the closed paths of integration in (3). It is interesting that the difference between the streamfunction values for Australia from the 12-month and 3-month average HR winds is small, but that the streamfunction value for New Zealand from the 3-month average HR winds is less than half that from the 12-month average. To the degree that the HR winds and Sverdrup model are both accurate at these latitudes, this may have important implications about seasonal variability of the circulation in the Tasman Sea, which is presently not well known. It is noteworthy that a strong eastward zonal jet at the latitude of the northern tip of New Zealand (along the Tasman Front) such as that present in the Sverdrup circulation from both the SASS and HR winds has been observed by Stanton (1981).

The Sverdrup volume transport streamlines computed globally north of 55°S from the full 96-day average SASS wind stress curl data by the method described above are shown in the top panel of Fig. 12. (A method for computing the Sverdrup circulation south of 55°S has been suggested, but the Sverdrup streamlines are shown here only at latitudes north of 55°S for reasons discussed at the end of this section.) The results of the same calculation using the three-month (July–September) average wind stress curl computed from the smoothed HR wind stress fields are shown in the middle panel, and the differences between the two estimates of the Sverdrup circulation are contoured in the lower panel of Fig. 12. The arrows on all three figures indicate the directions of the volume transport. Note that the circulation in a basin is closed by balancing the meridional component of Sverdrup transport integrated across the basin by return flows in viscous western boundary currents which are not depicted in Fig. 12. Physically, the vorticity injected into the water column by the wind stress curl is dissipated in these western boundary currents.

It can be seen from Fig. 12 that both wind stress datasets give very similar circulation patterns everywhere except in the Southern Ocean. As noted by Godfrey (1989), the westward jet at about 35°S in the Atlantic is a highly unrealistic feature of the Sverdrup model; the model fails to reproduce the retroflection of the Agulhas Current south of Africa. Elsewhere, the circulation patterns are consistent with the known characteristics of the general circulation of the world ocean. Except in the far western regions of each basin (see discussion below), the volume transports north of about 35°S computed from the two wind stress curl fields generally agree to within a few sverdrups. An interesting feature of both calculations is the complex system of zonal flows in the equatorial Pacific. The westward transport of the North Equatorial Current is clearly present from both the SASS and HR data between about 15° and 20°N. The eastward transport of the Equatorial Countercurrent centered at about 10°N is also evident in both calculations. The SASS data indicate narrow bands of opposing westward and eastward transport on opposite sides of the equator. This feature is present in the calculation from HR winds as well, but is much more well defined from the SASS winds because of the narrow band of zero wind stress curl along the equator discussed previously in section 3 (see Fig. 6).

The poleward transports of the western boundary currents of all of the subtropical gyres (see Table 3) are about 10 Sv higher from the 3-month average HR winds than from the 96-day average SASS winds. Note that the locations at which the western boundary current transports are given in Table 3 are the latitudes of maximum difference between the values obtained from the 96-day SASS and 3-month HR wind fields; the differences are always smaller to the north and south of these latitudes. The systematic differences between the transports of the western boundary currents are

TABLE 2. The values of the streamfunction for New Zealand (ψ_{NZ}) and Australia (ψ_{AUS}) obtained by the island rule (see text) based on the 96-day average SASS (SASS3), 3-month average HR (HR3) and 12-month average HR (HR12) wind stress curl fields. Also shown are the values of ψ_{NZ} and ψ_{AUS} obtained from the 12-month average HR wind stress curl by deSzoeke (1987) and Godfrey (1989).

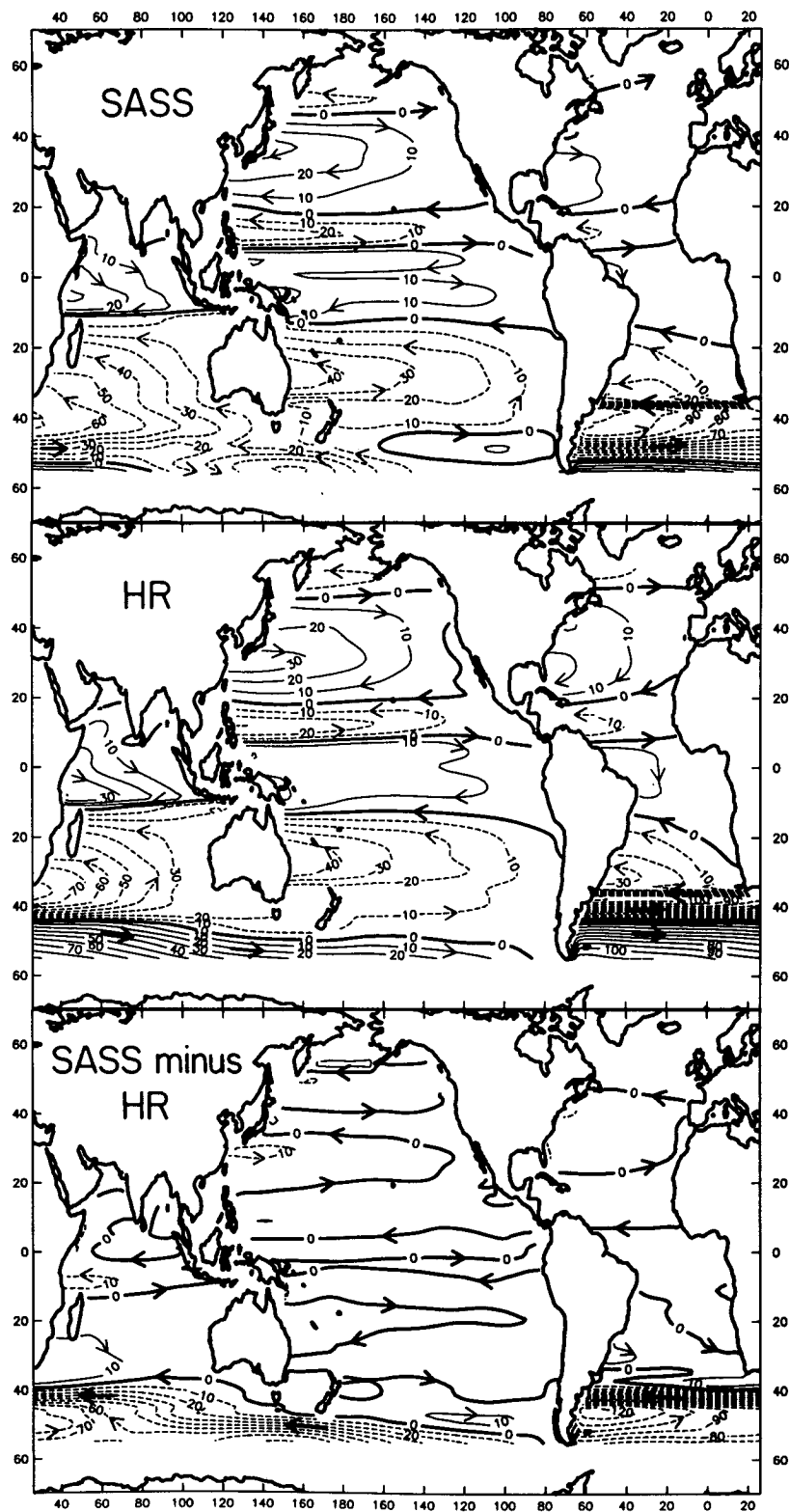|	ψ_{NZ}	ψ_{AUS}
SASS3	−9	−16
HR3	−12	−20
HR12	−28	−18
deSzoeke (1987)	−29	−17
Godfrey (1989)	−29	−16

FIG. 12. Sverdrup volume transport streamfunction in Sv computed from the 96-day average SASS (upper) and the July-August-September average HR (middle) wind stress curl fields. The difference between the two (SASS minus HR) is shown in the lower panel.

discussed further in section 6. [For comparison, the volume transports based on the annual average HR wind stress curl are also included in Table 3. These values sometimes differ by as much as a few sverdrups from those obtained by Hellerman and Rosenstein (1983) and Godfrey (1989) due to the smoothing applied here to the HR wind stress fields and to the different latitudes at which the transport values are determined.]

In contrast to the relatively small differences in the rest of the World Ocean, the two estimates of Sverdrup circulation differ enormously in the Southern Ocean. Throughout the region between 40° and 55°S, the eastward transport of the Antarctic Circumpolar Current (ACC) calculated from SASS winds is much lower than that calculated from the HR winds; across the width of the ACC, the eastward transport computed from SASS winds is more than 70 sverdrups less than that computed from the HR winds. The large differences are, of course, due to the very large differences between the SASS and HR wind stress fields discussed in section 4. The three-month average HR wind stress curl field is shown in Fig. 13, which can be contrasted with the 96-day average SASS wind stress curl field in Fig. 5. Also shown in Fig. 13 is the difference SASS minus HR wind stress curl. Differences are to be expected in the South Pacific where the meteorology was apparently somewhat anomalous in the 3-month average (Fig. 11). The meteorology was nearly normal in the South Atlantic and South Indian oceans, yet the line of zero SASS wind stress curl (corresponding to the location of the maximum eastward wind stress in the Southern Hemisphere westerlies) is everywhere poleward of the line of zero HR wind stress curl; the maximum latitudinal separations are in the South Atlantic and South Pacific, where the differences exceed 5° (see also Fig. 16 below). The SASS and HR wind stress curls thus differ in sign in this latitudinal band between the two lines of zero wind stress curl.

Although the Sverdrup model of wind-driven ocean circulation used here is exceedingly simple, it provides a measure of the sensitivity of ocean models to the differences between SASS and HR winds. The differences are likely to be at least qualitatively similar to Fig. 12 using more sophisticated ocean circulation models. A particularly striking discrepancy between the two estimates of Sverdrup circulation is the disagreement in the direction of the transport south of Australia and New Zealand. The calculation based on the 96-day average SASS wind stress curl indicates generally eastward transport except for a broad band of westward transport as far south as 55°S in the region from about 100°E to 140°W; the mean axis of the eastward ACC is evidently south of 55°S in this calculation. The calculation based on the 3-month average HR wind stress curl results in eastward transport everywhere, which is more consistent with the conventional view of the circulation in the Southern Ocean. It is noteworthy, however, that the Sverdrup circulation based on the 12-month average HR wind stress curl indicates westward transport as far south as 45°S in the region between about 110° and 150°E (Godfrey 1989). While not as extensive as from the SASS data, this tendency for westward transport indicates that the feature in the SASS wind stress curl field responsible for westward transport (i.e., a poleward displacement of the line of zero wind stress curl in the South Pacific) is also present to some degree in the annual average HR winds. The period of the SASS observations coincides with austral winter when the HR winds are least reliable. It would therefore not be surprising to find the climatological line of zero wind stress curl mislocated in the July–September average HR data.

The suggestion of westward transport south of Australia and New Zealand is rather surprising. Could it be that the conventional view of the circulation in the Southern Ocean is this much in error? It should be kept in mind that this Sverdrup calculation is based on only three months of wind stress data and an equilibrium Sverdrup balance on such short time scales could only be achieved if the variability of the circulation is barotropic. If a full year or more of scatterom-

TABLE 3. Transports in Sv ($=10^6$ m^3 s^{-1}) of the major western boundary currents (positive northward) and the Drake Passage and Indonesian throughflows (positive eastward) computed from the 96-day average SASS (SASS3), 3-month average HR (HR3) and 12-month average HR (HR12) wind stress curl fields. Also shown is the difference SASS3 minus HR3 (DIFF3). The latitudes indicated correspond to the location of maximum difference in each boundary current. The longitudes represent the westernmost grid point at which SASS wind stress curl values are available at the corresponding latitude. For reasons discussed in Chelton et al. (1989), the SASS winds analyzed here are not generally available closer than 500 km from land.

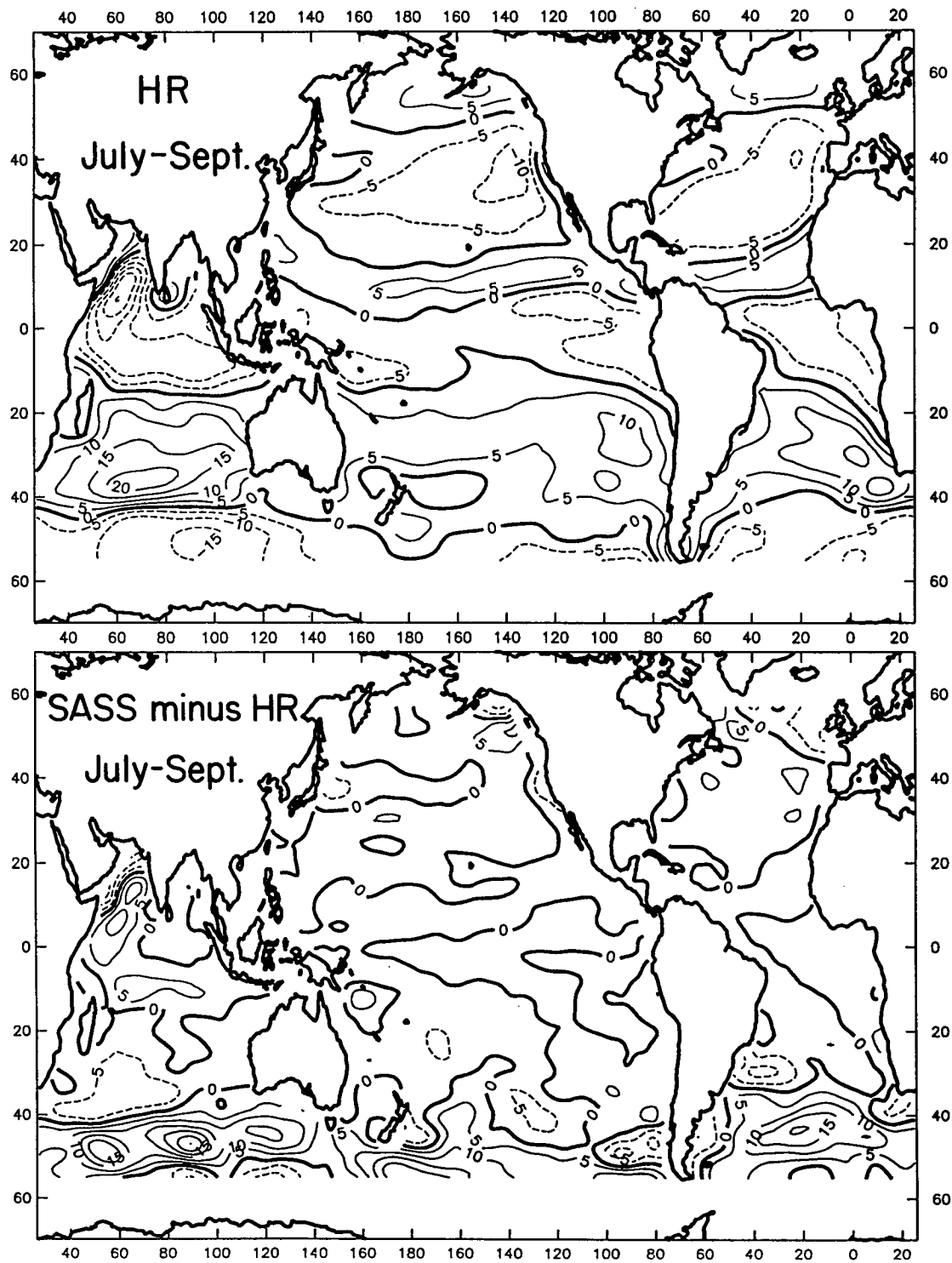| Current	Latitude	Longitude	SASS3	HR3	DIFF3	HR12
Gulf Stream	29°N	77°W	14	23	−9	29
Kuroshio	29°N	123°E	23	34	−11	55
Brazil	31°S	49°W	−22	−36	14	−30
East Australia	20°S	153°E	−34	−41	7	−20
Northern Somali	7°N	53°E	12	16	−4	2
Southern Somali	7°S	43°E	30	39	−9	26
Agulhas	31°S	33°E	−44	−56	12	−46
Drake Passage	55°S	29°W	44	110	−66	114
Indonesian throughflow	12°S	125°E	−16	−20	4	−18

Wind Stress Curl

FIG. 13. HR climatological average wind stress curl for the 3-month period July-August-September (upper) and the difference between the 96-day average SASS and the 3-month average HR wind stress curls (SASS minus HR) in units of 10^{-9} dyn cm^{-3}.

eter winds were available, the Sverdrup circulation computed from the long-term average wind stress field might look quite different from that computed from the 96-day SASS winds. The circulation south of Australia and New Zealand might also differ significantly using a more sophisticated model forced by the 96-day SASS winds. It is also likely that the westward flow computed from the SASS data is somewhat more intense than normal because of the apparently anomalous atmospheric blocking pattern southeast of New Zealand during the three-month averaging period July–October 1978 (see Fig. 11).

Despite all of these obvious limitations, there is evidence from historical hydrographic data to support the existence of westward transport south of Australia and New Zealand. Wyrtki (1971) computed the volume transport above and relative to 3000 m for the Indian Ocean (Fig. 14). The surface relative velocity and volume transport were both westward between Australia and about 45°S as far west as about 75°E. Reid (1986) estimated the total volume transport for the South Pacific Ocean (Fig. 15). The surface velocity was westward between Australia and about 40°S and there was westward volume transport west of about 155°W and as far south as about 50°S. Although not as extensive as the westward transport indicated in the SASS Sverdrup circulation (in which the westward transport extends all the way to 55°S and as far east as about 140°W), both historical hydrographic datasets show a clear tendency for westward transport in the region south of Australia and New Zealand.

Additional hydrographic data or reanalysis of historical hydrographic data are needed to yield further insight into the extent of the westward transport in the region south of Australia and New Zealand. Although the validity of the Sverdrup model and the applicability of such a model using only a 3-month average wind stress dataset are certainly issues here, the remarkably different circulation inferred from the SASS wind stress curl data has possibly important implications about wind-forced circulation in the Southern Ocean. It can be anticipated that the differences between the SASS

and HR wind fields would also have a large impact on the circulation estimated from more realistic ocean models. The existing hydrographic evidence for westward flow south of Australia and New Zealand from historical hydrographic data supports the suggestion in section 4 that the HR wind stress estimates may be systematically in error south of 45°S. A quantitative assessment of the reliability of climatological wind fields is therefore crucial for modeling the circulation of the Southern Ocean. At the very least, the Sverdrup calculation presented here may be evidence that the westward flow south of Australia and New Zealand is stronger during anomalous meteorological conditions.

A feature of considerable recent oceanographic interest (e.g., Gordon 1986) that can be estimated from the Sverdrup circulation is the transport from the Pacific to the Indian Ocean through the Indonesian passageway. The use of the island rule provides an immediate estimate of this transport. Since the north side of the passage represents a continuation of the eastern boundary of the Indian Ocean, the value of the streamfunction there is zero. Then, according to (2b), the transport through the passage is just equal to the island value of the streamfunction for Australia (see Table 2). The resulting Sverdrup estimates of Indonesian throughflow from the SASS and HR wind stress fields are listed in Table 3. The transports computed here from the 3-month average and annual average HR winds are 20 and 18 Sv, respectively, from the Pacific to the Indian Ocean. [For comparison, the estimates obtained by deSzoeke (1987) and Godfrey (1989) from the annual average HR winds are 17 and 16 Sv, respectively.] The SASS estimate is 16 Sv, which is somewhat lower than the 3-month HR estimate of 20 Sv. Direct estimates of Indonesian throughflow (reviewed by Gordon 1986) all indicate transport from the Pacific to the Indian Ocean, but with a rather broad range from 5 to 14 Sv. A more refined estimate of this transport can be expected from the observational component of the World Ocean Circulation Experiment.

Also of enduring oceanographic interest is the transport through Drake Passage. Stommel (1957) suggested
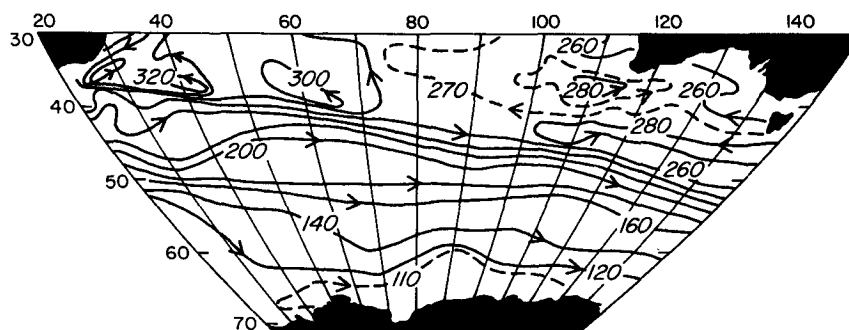

FIG. 14. Integrated volume transport streamfunction in Sv for the upper 3000 m relative to 3000 m for the South Indian Ocean (after Wyrtki, 1971).
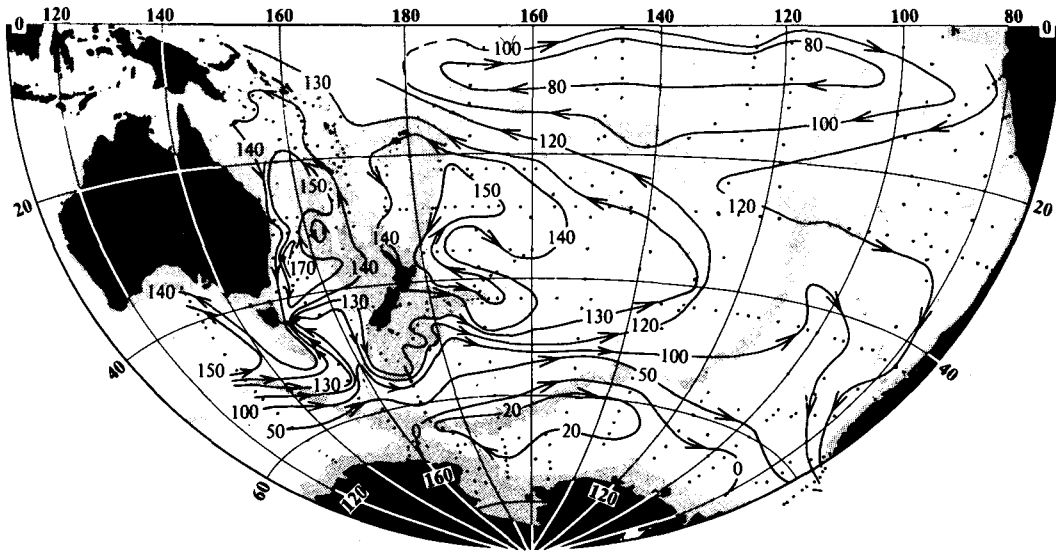
FIG. 15. An estimate of the total integrated volume transport streamfunction
in Sv for the South Pacific Ocean (from Reid 1986).

a method of continuing the calculation of the Sverdrup circulation at latitudes south of 55°S beyond the southern limit of the eastern boundary in the Pacific Ocean. The method is based on the observation that the latitude circles passing through Drake Passage between Cape Horn and the Antarctic Peninsula are all blocked by the Scotia Island Arc about 2200 km to the east so that there is no latitude with water deeper than 1000 m. The Scotia Island Arc can therefore be used as an eastern boundary to initiate the zonal integration of the wind stress curl and compute the Sverdrup circulation at latitudes south of Cape Horn. In this model of the circulation, the vorticity input to the water column by the wind stress curl would be dissipated in a viscous northward "boundary current" between Drake

Passage and the Scotia Island Arc. Observational evidence supports the existence of such a current: after passing through Drake Passage, nearly all of the transport of the ACC turns north before turning east again at about 40°W.

As a first-order test of the validity of the Sverdrup balance in the Southern Ocean, the relation between the wind stress curl and the location of the mean axis of the ACC can be examined. If the dynamics are Sverdrup-like, one would expect the viscous northward boundary current to "separate" and turn eastward approximately along the line of maximum wind stress (the line of zero wind stress curl) where no new vorticity is injected into the water column by the wind. (The exact location of the separation likely also depends on
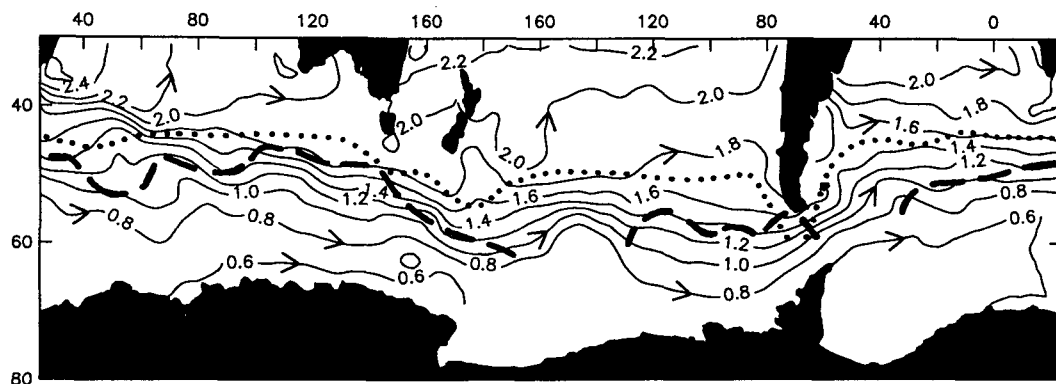

FIG. 16. The long-term average dynamic height in m of the sea surface relative to 2000 db (from Gordon and Molinelli 1982) for the Southern Ocean. The mean axis of the Antarctic Circumpolar Current coincides with the region of highest gradients of dynamic height. The dashed line corresponds to the line of zero wind stress curl from the 96-day average SASS data (from Fig. 5); the dotted line is the annual average HR line of zero wind stress curl.

the bathymetry.) As shown in Fig. 16, there is, in fact, generally good agreement between the line of zero SASS wind stress curl (dashed line) and the location of the mean axis of the ACC around the Southern Ocean as determined from the Gordon and Molinelli (1982) subjectively-contoured historical hydrographic data. (Note that there is no indication in this hydrographic data of the westward flow evident in Figs. 14 and 15 south of Australia and New Zealand, probably due to the subjective contouring applied by the authors.) By comparison, the line of zero wind stress curl from the annual-average HR data (which is very nearly coincident with the line of zero wind stress curl from the 3-month average HR winds) is everywhere considerably north of the mean axis of the ACC (see Fig. 16). The close relation between the mean axis of the ACC and the SASS winds is made all the more impressive by the fact that the SASS data span only a 3-month period and that topographic control of the flow of the ACC seems to be important in much of the Southern Ocean (Gordon et al. 1978; Chelton et al. 1990). Perhaps the wind stress curl field prescribes the approximate latitude of the ACC, and the detailed circulation is then modified by the bathymetry.

If a Sverdrup balance is indeed valid south of 55°S, then the transport through Drake Passage (which feeds the viscous northward current) must be balanced by general southward flow around the remainder of the circumpolar region. This total southward flow can be computed from the zonal integral of the wind stress curl. The transport through Drake Passage has been estimated from current meter data, bottom pressure measurements, and hydrographic sections to be 123 ± 30 Sv (Whitworth 1983; Whitworth and Peterson 1985). Using climatological wind stress from Han and Lee (1981), Baker (1982) computed a circumpolar southward transport of 190 Sv around the 55°S latitude circle, which is about 50% too high but with large uncertainty due to the questionable reliability of the climatological winds used in the calculation. More recently, Godfrey (1989) used the annual average HR wind stress curl to compute a circumpolar integrated southward transport of 128 Sv at 54°S. This value is remarkably close to the measured transport through Drake Passage. Using the HR wind stress data, we compute a southward Sverdrup transport across 55°S of 110 Sv from the July–September average and 114 Sv from the annual average (Table 3). The 14 Sv difference between our annual average estimate and that obtained by Godfrey (1989) is due to the smoothing applied here to the wind stress fields and the 1° difference in latitude used in the calculations. At latitude 55°S, the circumpolar southward transport computed from the SASS winds is only 44 Sv, which is too small by about a factor of three. Although the SASS winds are of much higher quality than the HR winds at this latitude, the 96-day duration of the dataset is too short to draw definitive conclusions about the validity of the

Sverdrup balance south of Cape Horn. We have therefore computed the global Sverdrup circulation shown in Fig. 12 only at latitudes north of 55°S.

6. The Hellerman and Rosenstein drag coefficient

As discussed in section 5, the western boundary current transports computed from the 3-month average HR data are systematically higher than those computed from the 96-day average SASS data (Table 3). As will become apparent in this section, these differences are a consequence of small systematic differences between the magnitudes of the wind stress values in the HR and SASS datasets. The systematic error is not obvious from the August and September differences between SASS and HR wind stress in Fig. 10 because the magnitude of the error is small compared with the differences between the climatological monthly average and an individual monthly average. The error becomes more apparent when the wind stress fields are averaged over longer periods and larger areas. From latitudinal profiles of the zonally-averaged eastward component of 3-month vector average wind stress (Fig. 17), for example, it is evident that the HR wind stress magnitudes are consistently higher than the SASS magnitudes in all of the major wind belts. Except south of 20°S where the HR wind stress fields are suspect (section 4), the zero crossings of the SASS and HR profiles are at the same latitudes. The westerly and easterly wind belts are all stronger in the HR dataset than in the SASS dataset. The nature of the systematic difference
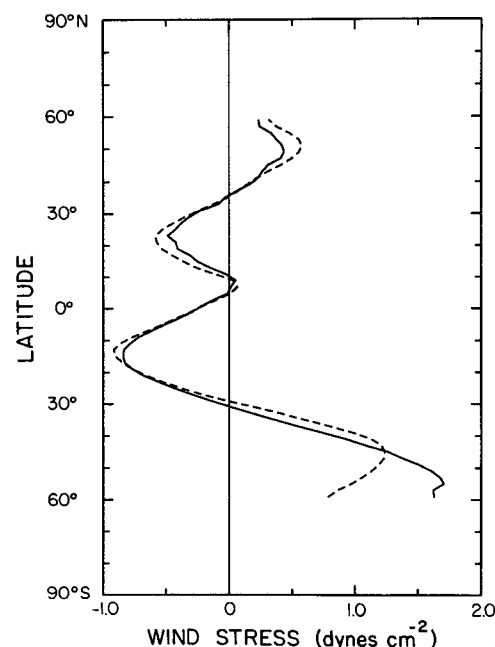

FIG. 17. Latitudinal profiles of zonally averaged eastward component of wind stress from the 96-day average SASS (continuous line) and 3-month average HR (dashed line) datasets.

between the two wind stress magnitudes is thus a multiplicative scaling factor (as opposed to a simple bias). The wind stress curls computed from the two datasets therefore also differ by a multiplicative scaling factor. When integrated across the basin using (1), the small systematic errors accumulate and result in western boundary current transports that are systematically higher from the HR than from the SASS wind stress curl fields.

There are a number of possible explanations for the discrepancies between the SASS and HR wind stress magnitudes. The systematic differences may be due to climatologically abnormal winds in every major wind belt during the Seasat mission, but this seems unlikely. Based on extensive comparisons between SASS and in situ winds, there is no evidence to suspect that SASS estimates of wind speed are systematically low. A more likely explanation is systematic differences between the drag coefficients used to compute the wind stress from vector winds by the bulk parameterization (see Appendix). The drag coefficient used here with the SASS data is the Large and Pond (1981) formulation. The drag coefficient used by Hellerman and Rosenstein (1983) is based on a least squares biquadratic fit of the drag coefficient as a function of wind speed and stability, using data provided by Bunker (1976). Careful inspection of Fig. 3 of Hellerman and Rosenstein (1983) reveals a reasonably good fit to the table at high wind speeds (greater than about 10 m s^{-1}). At lower wind speeds, however, which is the most important region of the table since this is the range of wind speeds most frequently observed over the ocean, the least squares fit gives drag coefficient values that are too high. The least squares fit evidently used uniform weighting, rather than weighting the more reliable portion of the table more heavily.

The magnitudes of the gridded HR and SASS 3-month vector average wind stress values north of 20°S are compared in Fig. 18. Interannual variability in the wind stress field can account for some of the scatter. Nonetheless, a scaling difference with no appreciable bias is clearly evident. The slope of a least-squares fit straight line through the origin is 1.19 ± 0.01, indicating that the HR wind stress magnitudes are about 19% higher than the SASS wind stress magnitudes. The solid line in Fig. 18 shows the relationship between wind stresses computed using the HR (ordinate) and Large and Pond (1981) (abscissa) drag coefficients. It is apparent that the systematic component of differences between HR and SASS wind stress (the quadratic tendency of the scatter plot) is almost entirely accounted for by the known differences between the two drag coefficients. The random scatter about the approximately quadratic systematic tendency represents the climatologically anomalous characteristics of the wind stress field during the Seasat observational period.

Although there is some uncertainty in the accuracy of the Large and Pond (1981) drag coefficient used
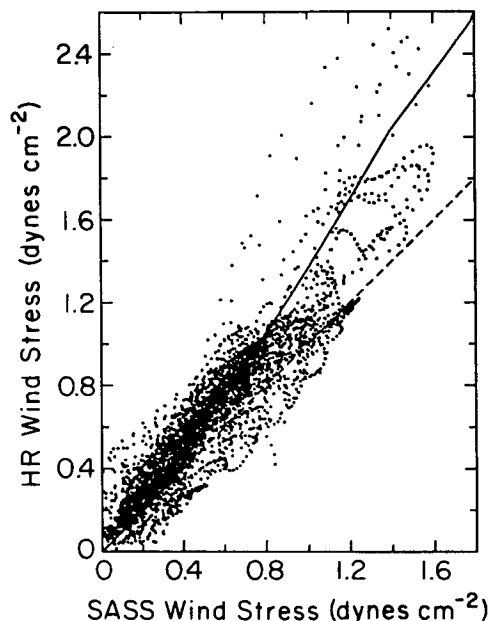

FIG. 18. Scatter plot comparison of HR 3-month average and SASS 96-day average wind stress magnitudes (smoothed as described in the Appendix) for latitudes north of 20°S. The perfect fit line with slope of 1 is shown by the dashed line. The solid line corresponds to the relation between wind stresses computed from the same wind speed for wind speeds from 0 to 11 m s^{-1} using the HR (ordinate) and Large and Pond (1981) (abscissa) drag coefficients.

here, the discrepancies between the HR drag coefficient and the table of Bunker (1976) suggest that the HR drag coefficient is probably too large. This conclusion is supported by recent modeling results obtained by P. Schopf (personal communication 1989), who finds better agreement between modeled and observed sea level in the tropical Pacific when the HR drag coefficient is reduced by 17%, which is very close to the straight-line fit value of 19% obtained here. A recalculation of climatological global wind stress by Harrison (1989) from essentially the same surface marine dataset used by HR, but with Large and Pond drag coefficient, also concludes that the HR drag coefficient is too large by about 20%. The same conclusion has been reached by Trenberth et al. (1989). While there is general agreement that the HR drag coefficient is too high, the effects of this error on the HR climatological monthly-average wind stress fields has perhaps not been fully appreciated. Indeed, it has been speculated that the high drag coefficient may, in some way, compensate for undersampling of high winds because of geographical biases in ship observations. Figure 18 shows that this is clearly not the case.

7. Operational analyses of near-surface winds

Near-surface wind fields produced by operational meteorological forecast and analysis models offer an attractive alternative source of wind data for forcing

ocean models and constructing global climatological wind fields (see, e.g., Trenberth et al. 1989). The meteorological analyses blend observations with estimates of the dynamics to generate wind fields on a regular space–time grid. Operational wind analyses are known to be inaccurate in the tropics (Reynolds et al. 1989; Trenberth et al. 1989). Outside of the tropics, recent operational analyses by ECMWF and NMC compare well with observations wherever observations exist. There is a temptation, then, to believe that the analyses are also accurate in data-sparse regions. It is well to keep in mind, however, that the analyses in such regions rely heavily on the estimates of the dynamics incorporated in the model. The analyses are therefore presumably less accurate in the Southern Hemisphere than in the Northern Hemisphere because of the extremely uneven distribution of available land and ship observations; the Southern Hemisphere accounts for over two-thirds of the surface area of the world ocean, but only one-fifth of the total number of ship observations over the past 100 years. It has been difficult to quantify such geographically dependent errors since most of the direct observations that would be used to test the analyzed fields are already incorporated in the analyses through the data assimilation schemes. Satellite scatterometry probably offers the only means of globally assessing the quality of operational analyses.

There are no satellite scatterometer data from which present-day operational analyses can be evaluated. The next satellite scatterometer has an expected launch date in 1991 onboard the ERS-1 satellite. The three months of SASS winds analyzed here constitute the only high-quality, independent global dataset with which to evaluate the quality of wind fields from contemporaneous operational analyses. Although there is little doubt that the many changes introduced in operational forecast and analysis schemes since the Seasat mission (see, e.g., Trenberth and Olson 1988) have considerably improved the quality of the near-surface wind analyses, the comparisons with analyses during 1978 arguably still draw attention to potential problems in present-day operational analyses.

Twice-daily (0000 and 1200 UTC) NMC global 1000 mb wind analyses on the 2.5°-square grid were extrapolated to the SASS 19.5 m reference height using a simple atmospheric boundary layer parameterization that reduced and rotated the 1000 mb winds in a manner determined from simulations to be statistically appropriate (G. Levy, personal communication 1988; Brown and Liu 1982). Poleward of 15° latitude, the 1000 mb winds were reduced by 30% in magnitude and rotated 14° counterclockwise (clockwise) in the Northern (Southern) Hemisphere. (This turning angle is smaller than that generally used because the reference height is 19.5 m rather than the more commonly used 10 m.) Equatorward of 15° latitude, the rotation was decreased linearly to zero at the equator and the 30% reduction was held constant. Gridded fields of wind

stress were computed at each analysis time using the bulk parameterization described in the Appendix, and the twice-daily wind stress fields were averaged over the SASS monthly periods (Table 1). No additional smoothing was applied to the averaged NMC wind stress fields, which were then subtracted from the SASS data in Fig. 1 to obtain the difference maps shown in Fig. 19.

The SASS and NMC wind stress fields generally agree to within 0.2–0.3 dyn cm^{-2} everywhere north of 20°N, except during September in the North Atlantic where the NMC analyses failed to predict accurately the strong QE-II storm and the increased strength of the westerlies north of 55°N discussed in section 3. Otherwise, there is a distinct asymmetry about the equator in the quality of the tropical NMC winds; with the exception of the region around the Hawaiian islands, NMC errors are seldom as large as 0.3 dyn cm^{-2} north of the equator, but are commonly larger in the Southern Hemisphere. The close agreement between SASS and NMC average stress fields in the data-rich regions of the Northern Hemisphere suggests that the NMC operational products during the Seasat period were reasonably accurate on monthly time scales north of 20°N.

In the tropics, the NMC analyses underestimated the strength of the southeast tradewinds (especially in the Indian Ocean) and failed to resolve the narrow parallel bands of light winds and strong southerly winds straddling the equator in the eastern tropical Pacific (Fig. 6). The large errors near Hawaii extend over 60°–80° of longitude and 15° of latitude and are generally larger westward (downwind) of the islands. As the NMC analyses incorporated radiosonde measurements from Hawaii, it appears that these in situ data are not representative of open ocean conditions, perhaps due to direct orographic effects or to diurnal wind variations associated with the presence of the large islands.

The largest differences between NMC and SASS average fields occur in the high southern latitudes where NMC analyses prior to 1982 are known to be poor (Trenberth and Olson 1988). The NMC analyses consistently underestimated the westerly vector averaged wind stress south of 45°S by more than 1 dyn cm^{-2}, and completely missed the dramatic increase in winds in the South Pacific sector between August and September.

The comparisons between SASS and NMC operational analyses thus generally validate the Northern Hemisphere midlatitude monthly mean surface stress fields constructed from 1978 NMC data. The poor agreement in the tropics and the Southern Hemisphere is clear indication that the contemporaneous operational analyses were inaccurate in these data-sparse regions. If the quality of present-day operational analyses has improved globally to the level where they were accurate regionally in 1978, then these analyses should be adequate for modeling the global ocean circulation.

SASS minus NMC Wind Stress

September

July

July–
September

August

CHELTON, MESTAS-NUÑEZ AND FREILICH
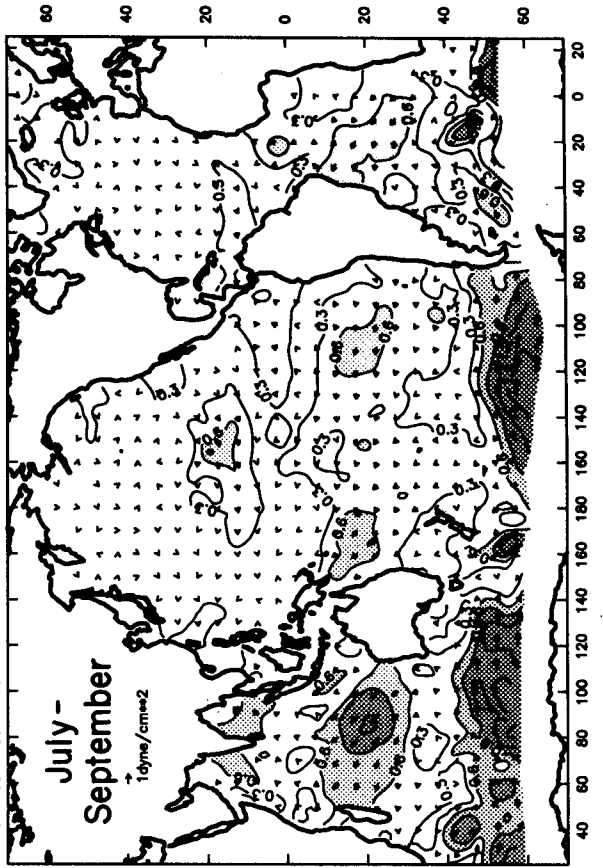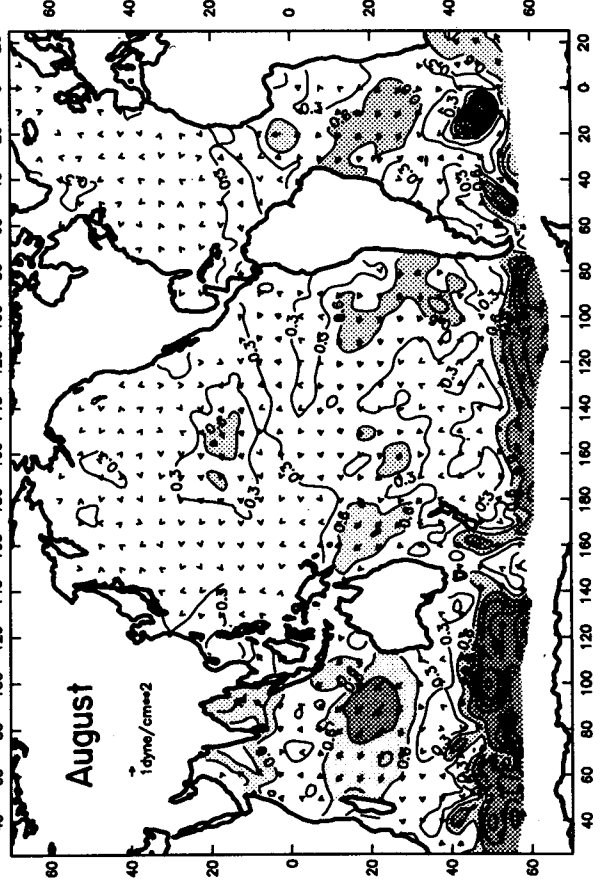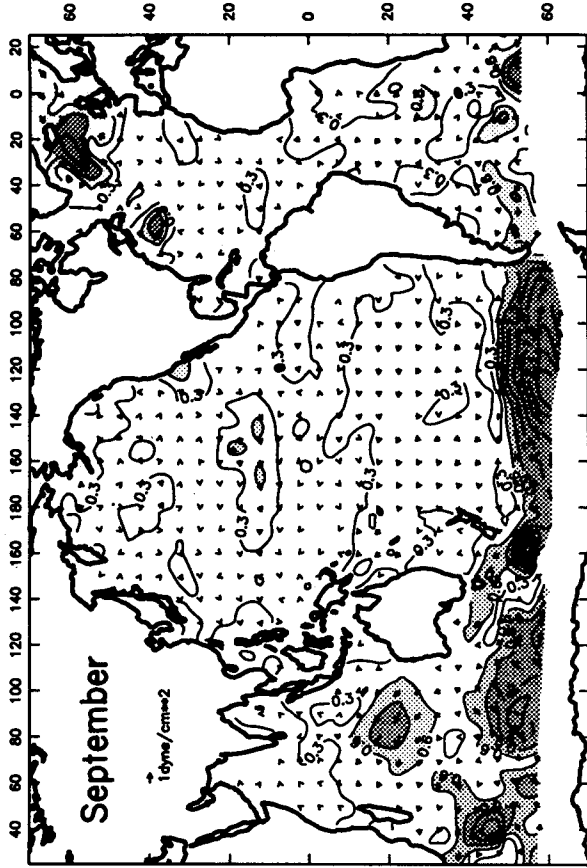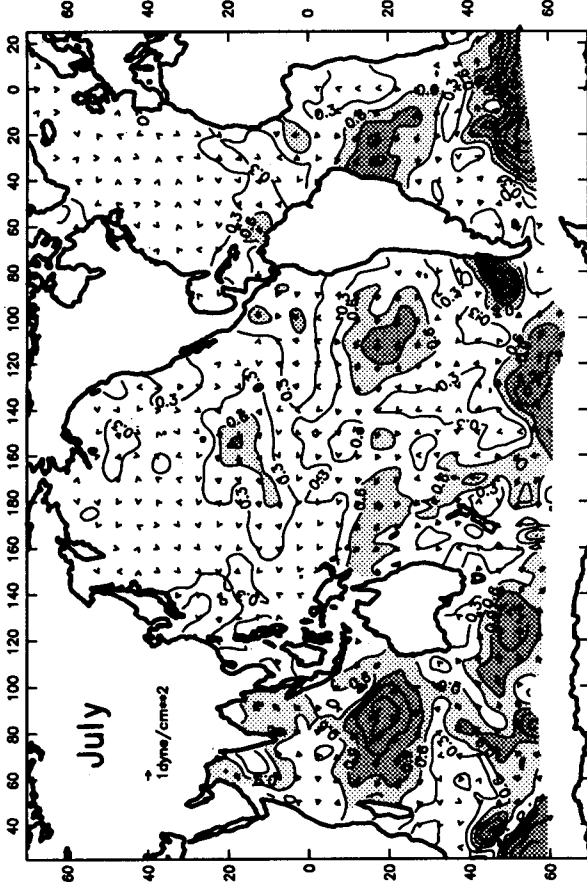
To the degree that operational analyses are still dependent on in situ observations, however, regional discrepancies between the SASS and 1978 NMC analyses such as the large errors near Hawaii and the poor analysis of the *QE-II* storm may still exist in refined, present-day operational analyses, especially at high southern latitudes. An accurate scheme for assimilating near-real-time scatterometer data into operational meteorological analyses could greatly improve the quality of the resulting surface wind fields (Cane et al. 1981; Yu and McPherson 1984; Duffy and Atlas 1986).

8. Conclusions

Global vector wind observations from the Seasat-A Satellite Scatterometer (SASS) have been analyzed for the period 7 July–10 October 1978 (the duration of the Seasat mission) to describe the global monthly average wind stress and wind stress curl fields. Efforts to use the SASS data to validate present-day operational analyses of near-surface winds were frustrated by the poor quality of NMC analyses over much of the world ocean during the period of the Seasat mission. With the many changes (presumably improvements) introduced in the operational analysis procedures during the decade since the Seasat mission, the quality of present-day analyses may have improved to a level acceptable for ocean modeling. Contemporaneous satellite scatterometer data from the European Space Agency and NASA scatterometers to be launched in 1991 and 1995, respectively, will provide the only means of globally assessing the quality of state-of-the-art operational analyses.

Comparisons between SASS and HR climatological average wind stress fields found the two to be surprisingly similar north of 35°S, with the differences generally consistent with plausible interannual variability of the surface wind field; with a few exceptions, the wind stress field during the Seasat mission evidently did not deviate greatly from the climatological normal north of 35°S. At higher southern latitudes, where historical observations from ships are sparse and the HR wind stress fields are based largely on U.S. Navy wind rose data rather than direct observations, the magnitudes and spatial extent of the discrepancies between SASS winds and climatological averages are larger than we feel can reasonably be ascribed totally to deviations of the Seasat observational period from the climatological norm. The quality of the HR wind fields is therefore suspect over the Southern Ocean. Based on operational analyses of sea level pressure by the Australian Bureau of Meteorology, somewhat anomalous

meteorological conditions appear to account for part of the discrepancies between SASS and HR winds in the high-latitude South Pacific.

As a first-order measure of the sensitivity of wind-driven models of ocean circulation to the differences between the SASS and HR winds, the Sverdrup circulation was computed globally north of 55°S from the 96-day average SASS and 3-month average HR wind stress curl fields. North of 35°S, the two estimates of Sverdrup circulation generally agree to within a few sverdrups. The poleward transports of all major western boundary currents are about 10 Sv higher from the HR winds than from the SASS winds. This systematic difference is due to differences between the drag coefficient used by Hellerman and Rosenstein (1983) and the Large and Pond (1981) drag coefficient used here; the HR formulation is too high by about 19%.

In the Southern Ocean, differences in Sverdrup circulation are exceptionally large. The two estimates of transport across the ACC differ by more than 70 Sv. Moreover, they even disagree in the direction of the transport in the region south of Australia and New Zealand. The westward transport indicated by the SASS data contradicts the traditional view that the transport is eastward throughout the Southern Ocean (except very close to the Antarctic continent). Notwithstanding the obvious limitations of the Sverdrup model and the fact that meteorological conditions were somewhat anomalous southeast of New Zealand over the three-month averaging period July–October 1978, there is evidence in the historical hydrographic data to support the existence of westward transport south of Australia, although not as extensive as indicated from the Sverdrup model and SASS wind stress field. The analysis presented here may be evidence that the westward flow is stronger in some years than in others.

The nature of the circulation south of Australia and New Zealand is a research topic worthy of further investigation from historical hydrographic data or new hydrographic and current meter measurements that may be collected as part of the World Ocean Circulation Experiment. For present purposes, however, the important point is that the circulation patterns estimated from the two wind stress datasets are undeniably different. We conclude that reliable estimates of the wind stress field over the Southern Ocean are imperative for accurate models of the global ocean circulation. In view of the suspected large errors in the HR wind stress fields over the Southern Ocean, it may be better to use SASS wind stress fields (or some suitably smoothed versions thereof) than the climatological averages to force ocean models. Otherwise, the line of

FIG. 19. As in Fig. 10, except differences between monthly vector averages and the vector average over the full Seasat mission of wind stress computed from SASS data and operational analyses from the National Meteorological Center (NMC) for the periods listed in Table 1. The NMC 1000 mb winds were converted to wind stress as described in the text. The SASS data were smoothed as described in the Appendix, but no smoothing was applied to the NMC data.

zero wind stress curl may be mislocated and the magnitude of the positive wind stress curls on the northern side of the Southern Hemisphere westerlies could be significantly underestimated, thus leading to errors in the location and transport of the ACC.

APPENDIX

Averaged SASS Wind Stress Fields

The procedure used to construct monthly average wind stress and wind stress curl fields from SASS data is summarized in this appendix. For each individual SASS vector wind observation, the wind stress τ was computed using the bulk parameterization

$$\tau = \rho_a C_D v_{10} \mathbf{v}_{10}, \qquad (6)$$

where ρ_a is the air density, C_D is the drag coefficient, $\mathbf{v}_{10}$ is the vector wind at a height of 10 m above the sea surface and v_{10} is the scalar wind speed at 10 m. The air density was assigned a constant value of $\rho_a = 1.223 \times 10^{-3}$ g cm^{-3}. This use of a constant density introduces a small systematic error (less than 5% over the latitude range analyzed here) because of the temperature dependence of air density. This could be improved by adjusting ρ_a for climatological average surface air temperatures, but some residual error would still exist because of variability of surface air temperature on synoptic and interannual time scales.

The SASS measurements of radar backscatter are calibrated to estimate the neutral-stability vector wind at a height of 19.5 m above the sea surface (Schroeder et al. 1982). In other words, the scatterometer algorithm estimates the wind velocity at 19.5 m required to produce the actual surface stress if the atmospheric stratification was neutrally stable. Since the effects of atmospheric stability have thus been implicitly incor-

porated in the SASS wind vector algorithm, the appropriate estimate of wind stress from SASS winds is computed from (6) using the neutral-stability drag coefficient. The wind-speed dependent drag coefficient suggested by Large and Pond (1981) was used here, with the low wind speed branch arbitrarily extended to include wind speeds in the range 0–4 m s^{-1},

$$10^3 C_D = \begin{cases} 1.14 & \text{if } v_{10} \leqslant 10 \text{ m s}^{-1}; \\ (0.49 + 0.065 v_{10}) & \text{if } v_{10} > 10 \text{ m s}^{-1}. \end{cases}$$

$$(7)$$

The 19.5 m neutral-stability SASS wind speeds $v_{19.5}$ were reduced to a reference height of 10 m by

$$v_{10} = 0.943 v_{19.5}, \qquad (8)$$

where 0.943 is the neutral-stability correction factor.

The use of the drag coefficient formulation (7) neglects the effects of random variations in the surface roughness length z_0 on the relation between neutral-stability wind and surface wind stress (systematic wind-speed dependent variations in z_0 are presumably implicitly incorporated in the drag coefficient C_D.) This source of random error is unavoidable in wind stress estimated from wind speed by bulk parameterization, but is significantly reduced by the averaging of many individual SASS estimates of wind stress (presumably over a wide range of z_0) in the monthly average wind stress fields analyzed here. It is noteworthy that Li et al. (1989) recently documented a case study from aircraft scatterometer measurements across a strong thermal front suggesting that radar backscatter is more closely related to surface wind stress than to the neutral-stability wind speed. It may therefore be possible in the future, after suitable algorithm development, to estimate surface wind stress directly from scatterometer measurements of radar backscatter, thus eliminating errors due to neglect of random variations in z_0.

For each monthly period and for the full 96-day Seasat mission (Table 1), the individual wind stress values computed from the SASS winds were vector averaged on a 2.5° latitude–longitude grid for the region from 70°S to 70°N. Data over land and poleward of the maximum northward extent of the Antarctic ice boundary during the Seasat mission (see Johnson 1986; Chelton et al. 1989) were excluded from the averages. The magnitude of the gridded monthly vector average wind stress was plotted as a global contour map and the contours exhibited some oscillatory behavior in the zonal direction with wavelength approximately equal to the separation between consecutive satellite ground tracks. This is undoubtedly due to spatial inhomogeneity of residual sampling errors in the monthly averages. Such behavior is not surprising in view of the fact that Seasat sampled some regions more frequently

than others with its nearly repeating orbit (exactly repeating during the last 25 days of the mission).

To remove the spatial variations in sampling error, some smoothing of the 2.5° averaged wind stress fields is necessary. The form of the low-pass filter used here consists of a two-dimensional tricubic weighted average in the spatial domain. For a scalar field (or a single component of a vector field) $f(x, y)$, the smoothed value at a point (x_0, y_0) is

$$\bar{f}(x_0, y_0) = \frac{1}{W} \sum_{i=1}^{N_x} \sum_{j=1}^{N_y} w_{ij} f(x_i, y_i), \qquad (9)$$

where

$$w_{ij} = \begin{cases} (1 - d_{ij}^3)^3, & \text{if } 0 \leq d_{ij} \leq 1 \\ 0, & \text{if } d_{ij} > 1 \end{cases}$$

$$d_{ij} = \left[\left(\frac{x_i - x_0}{h_x} \right)^2 + \left(\frac{y_j - y_0}{h_y} \right)^2 \right]^{1/2}$$

$$W = \sum_{i=1}^{N_x} \sum_{j=1}^{N_y} w_{ij}.$$

The filter parameters h_x and h_y (with the same units as the grid spacings Δx and Δy) are half of the total spans of the smoothing filter in the x and y directions, and N_x and N_y are the numbers of discrete points in the x and y directions within the spans of the filter.

A one-dimensional slice through this tricubic weighting function is shown graphically in Figure 20a. This filter is locally flat in the vicinity of the center point (x_0, y_0) and tapers smoothly to zero at distances of h_x and h_y from the center point in the x and y directions, respectively. The tapered edges have a value of 0.5 at distances of $0.59h_x$ and $0.59h_y$ from the center point in the x and y directions. The wavenumber transfer function of the tricubic low-pass filter is shown in Fig. 20b. For comparison, the simple running average filter and corresponding wavenumber transfer function are shown as dashed lines in Figure 20 for a filter half-span equal to the half-amplitude points of the tricubic filter. It is evident that the tricubic filter has much better characteristics in the wavenumber domain; sidelobe contamination is much smaller with very little sacrifice of wavenumber resolution in the low-pass wavenumber band. The half-power point of the transfer function of the one-dimensional tricubic filter is at a wavenumber of about $(2h_x)^{-1}$.

After some experimentation, it was found that most of the oscillatory behavior of contours that was symptomatic of sampling errors could be removed with tricubic filter parameters $h_x = 7°$ and $h_y = 3°$. With these filter parameters, the tricubic filter is analogous to a running average of dimensions 8.25° by 3.5°, and corresponds to a low-pass half-power cutoff at wavelengths of about 14° of longitude and 6° of latitude. The anisotropic form of the filter (longer zonal than meridi-
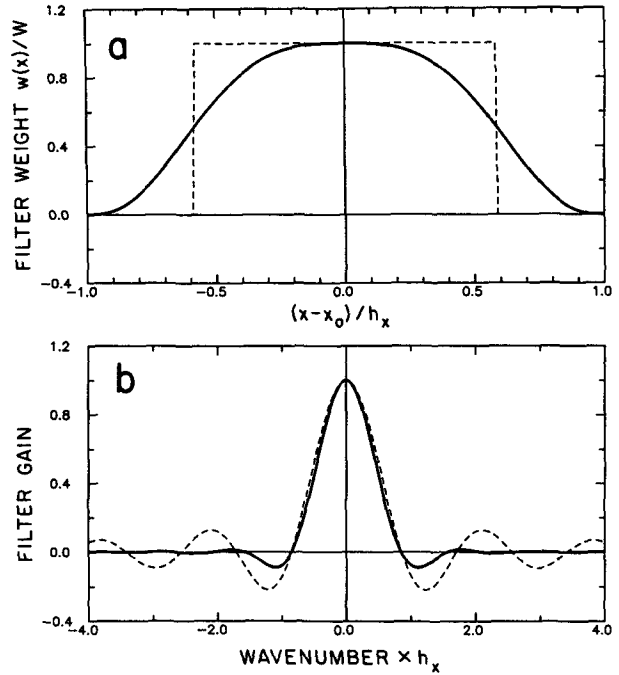

Fig. 20. Graphical representations of two low-pass filters: (a) the filter weights along the x-axis of the 2-dimensional filters; and (b) the gain of the corresponding transfer functions in the wavenumber domain. The heavy lines correspond to the tricubic filter described in the text with a half-span of h_x centered on x_0. The dashed lines correspond to the simple running average with a half-span of 0.59 h_x centered on the point x_0.

onal scale) was adopted to preserve a preconceived notion that wind fields are more coherent zonally than meridionally in monthly averages. These filter parameters were used in the tropical maps in Figs. 6–9. Values of $h_x = 7°$ and $h_y = 3°$ in global maps resulted in (probably real) structure in the contoured wind fields with too much detail to be discerned when reduced to the sizes in Figs. 2–5. Consequently, to make the global maps more legible, the 2.5° gridded averages were smoothed with tricubic filter parameters $h_x = 14°$ and $h_y = 4.5°$ (analogous to a running average of dimensions 16.5° by 5.3°). This degree of smoothing produced SASS wind fields consistent with the spatial scales resolvable by the NMC operational analyses (see section 7). The smoothed values at grid points near continental boundaries where some of the grid points within the span of the filter were missing were computed from the tricubic weighted average of all nonmissing grid points within the x and y spans of the filter. The same smoothing was applied both to the monthly averages and the 96-day average.

The wind stress directional steadiness, defined to be the ratio of the magnitude of vector averaged wind stress to the scalar averaged wind stress magnitude, was computed for each 2.5° region over the three monthly averaging periods and the full 96-day aver-
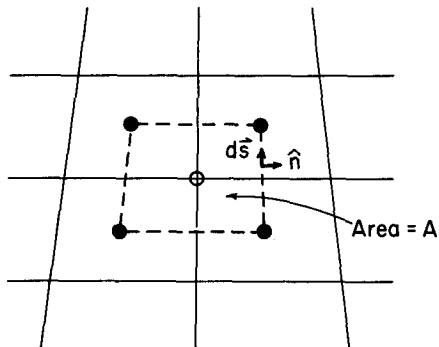
FIG. 21. Schematic diagram of the use of Stokes' Theorem to compute wind stress curl from gridded fields of wind stress. The solid lines represent the boundaries of the 2.5° averages of wind stress centered at the solid circles. (The convergence of meridional lines is due to the curvature of the earth's surface.) The 2.5° region centered at the open circle has area A and is bounded by the dashed lines with unit vector path element ds and unit outward normal $\hat{n}$.

aging period. The global 2.5° directional steadiness fields were then smoothed with the same low-pass filter applied to the global vector average wind stress fields.

The wind stress curl was computed from the smoothed vector-averaged wind stress field using Stokes' Theorem. The center points of four contiguous 2.5° average wind stress values mark the four corners of a 2.5° region (Fig. 21). If the average wind stress is assumed constant over this 2.5° region, the solution for the wind stress curl in the area is

$$\nabla_H \times \tau = \frac{1}{A} \oint \tau \cdot ds, \qquad (10)$$

where ∇_H is the horizontal del operator, ds is a unit vector parallel to the closed path around the perimeter of the area, and A is the area of the region. The values of the parallel component of wind stress $\tau \cdot ds$ along each side of the region (dashed lines) were taken to be the average of the corresponding component of the gridded values at the two adjacent corners of the region. Thus defined, the values of $\tau \cdot ds$ for the four sides of the region were summed and divided by the area A to obtain the wind stress curl. This method of curl calculation results in less degradation of the spatial resolution than does the more conventional centered first differences approach. Note that the grid centers of the wind stress curl fields computed in this manner are staggered relative to those of the wind stress field (Fig. 21).

REFERENCES

Atlas, R., A. J. Busalacchi, M. Ghil, S. Bloom and E. Kalnay, 1987: Global surface wind and flux fields from model assimilation of Seasat data. *J. Geophys. Res.,* **92**, 6477–6487.

Baker, D. J., 1982: A note on the Sverdrup balance in the Southern Ocean. *J. Mar. Res.,* **40**(Suppl.), 21–26.

Bunker, A. F., 1976: Computations of surface energy flux and annual air–sea interaction cycles of the North Atlantic Ocean. *Mon. Wea. Rev.,* **104,** 1122–1140.

Brown, R. A., and W. T. Liu, 1982: An operational large-scale marine PBL model. *J. Appl. Meteor.,* **21,** 261–269.

Bryan, K., and L. J. Lewis, 1979: A water mass model of the world ocean. *J. Geophys. Res.,* **84,** 2503–2517.

Cane, M. A., V. J. Cardone, M. Halem and I. Halberstam, 1981: On the sensitivity of numerical weather prediction to remotely sensed marine surface wind data: A simulation study. *J. Geophys. Res.,* **86,** 8093–8106.

Chelton, D. B., K. J. Hussey and M. E. Parke, 1981: Global satellite measurements of water vapour, wind speed, and wave height. *Nature,* **294,** 529–532.

——, M. H. Freilich and J. R. Johnson, 1989: Evaluation of unambiguous vector winds from the Seasat scatterometer. *J. Atmos. Oceanic Technol.,* **6,** 1024–1039.

——, M. G. Schlax, D. L. Witter and J. G. Richman, 1990: Geosat altimeter observations of the surface circulation of the Southern Ocean. *J. Geophys. Res.,* in press.

deSzoeke, R. A., 1987: On the wind driven circulation of the South Pacific Ocean. *J. Phys. Oceanogr.,* **17,** 613–630.

Duffy, D. G., and R. Atlas, 1986: The impact of Seasat-A scatterometer data on the numerical prediction of the Queen Elizabeth II storm. *J. Geophys. Res.,* **91,** 2241–2248.

Godfrey, J. S., 1989: A Sverdrup model of the depth-integrated flow for the world ocean allowing for island circulations. *Geophys. Astrophys. Fluid Dyn.,* **45,** 89–112.

Gordon, A. L., 1986: Interocean exchange of thermocline water. *J. Geophys. Res.,* **91,** 5037–5046.

——, and E. Molinelli, 1982: *Southern Ocean Atlas,* Columbia University Press. 34 pp. plus 248 plates.

——, E. Molinelli and T. N. Baker, 1978: Large-scale relative dynamic topography of the Southern Ocean. *J. Geophys. Res.,* **83,** 3023–3032.

Gyakum, J. R., 1983: On the evolution of the *QE-II* storm. I: Synoptic aspects. *Mon. Wea. Rev.,* **111,** 1137–1155.

Halpern, D., 1988: On the accuracy of monthly mean wind speeds over the equatorial Pacific. *J. Atmos. Oceanic Technol.,* **5,** 362–367.

Han, H.-J., and S.-W. Lee, 1981: A new analysis of monthly mean wind stress over the global ocean. *Rep. 26,* 148 pp., Clim. Res. Inst., Oregon State University.

Harrison, D. E., 1989: On climatological monthly mean wind stress and wind stress curl fields over the world ocean. *J. Climate,* **2,** 57–70.

Hawkins, J. D., and P. G. Black, 1983: Seasat scatterometer detection of gale force winds near tropical cyclones. *J. Geophys. Res.,* **88,** 1674–1682.

Hayes, S., M. J. McPhaden and J. M. Wallace, 1989: The influence of sea surface temperature on surface wind in the eastern equatorial Pacific: Weekly to monthly variability. *J. Climate,* **2,** 1500–1506.

Hellerman, S., 1967: An updated estimate of the wind stress on the world ocean. *Mon. Wea. Rev.,* **95,** 593–606. [See correction 1968, *Mon. Wea. Rev.,* **96,** 63–74.]

——, and M. Rosenstein, 1983: Normal monthly wind stress over the world ocean with error estimates. *J. Phys. Oceanogr.,* **13,** 1093–1104.

Johnson, J. R., 1986: Analysis of Seasat-A satellite scatterometer wind observations with emphasis over the Antarctic Circumpolar Current. M. S. thesis, Oregon State University, 260 pp.

Large, W. G., and S. Pond, 1981: Open ocean momentum flux measurements in moderate to strong winds. *J. Phys. Oceanogr.,* **11,** 324–336.

Legler, D. M., and J. J. O'Brien, 1984: Atlas of tropical Pacific wind-stress climatology, 1971–1980. Florida State University, 182 pp.

Li, F., W. Large, W. Shaw, E. J. Walsh and K. Davidson, 1989: Ocean radar backscatter relationship with near-surface winds: A case study during FASINEX. *J. Phys. Oceanogr.,* **19,** 342–353.

Luther, D. S., and D. E. Harrison, 1984: Observing long period fluctuations of surface winds in the tropical Pacific: Initial results from island data. *Mon. Wea. Rev.,* **112,** 285–302.

O'Brien, J. J., and S. B. Goldenberg, 1982: Atlas of tropical Pacific wind-stress climatology, 1961–1970. Florida State University, 182 pp.

Pedlosky, J., 1987: *Geophysical Fluid Dynamics.* Springer-Verlag, 710 pp.

Reid, J. L., 1986: On the total geostrophic circulation of the South Pacific Ocean: Flow patterns, tracers and transports. *Progress in Oceanography,* Vol. 16, Pergamon, 1–61.

Reynolds, R. W., K. Arpe, C. Gordon, S. P. Hayes, A. Leetma and M. J. McPhaden, 1989: A comparison of tropical Pacific surface wind analyses. *J. Climate,* **2,** 105–111.

Sadler, J. C., and B. J. Kilonsky, 1981: Trade wind monitoring using satellite observations. Rep. UHMET 81-01, Department of Meteorology, University of Hawaii.

Schroeder, L. C., D. H. Boggs, G. J. Dome, I. M. Halberstam, W. L. Jones, W. J. Pierson and F. W. Wentz, 1982: The relationship between wind vector and normalized radar cross section used to derive Seasat-A satellite scatterometer winds. *J. Geophys. Res.,* **87,** 3318–3336.

Semtner, A., and R. Chervin, 1988: A simulation of the global ocean circulation with resolved eddies. *J. Geophys. Res.,* **93,** 15 502–15 522.

Stanton, B. R., 1981: An oceanographic survey of the Tasman Front. *New Zealand J. Mar. Freshwater Res.,* **15,** 289–297.

Stommel, H., 1957: A survey of ocean current theory. *Deep-Sea Res.,* **4,** 149–184.

Trenberth, K. E., and K. C. Mo, 1985: Blocking in the southern hemisphere. *Mon. Wea. Rev.,* **113,** 3–21.

——, and J. G. Olson, 1988: An evaluation and intercomparison of global analyses from the National Meteorological Center and the European Centre for Medium Range Weather Forecasts. *Bull. Amer. Meteor. Soc.,* **69,** 1047–1057.

——, J. G. Olson and W. G. Large, 1989: A global ocean wind stress climatology based on ECMWF analyses. National Center for Atmos. Res. Tech. Note NCAR/TN-338 + STR, 93 pp.

Wallace, J. M., T. P. Mitchell and C. Deser, 1989: The influence of sea-surface temperature upon surface wind in the eastern equatorial Pacific: Seasonal and interannual variability. *J. Climate,* **2,** 1492–1499.

Whitworth, T., 1983: Monitoring the transport of the Antarctic Circumpolar Current at Drake Passage. *J. Phys. Oceanogr.,* **13,** 2045–2057.

——, and R. G. Peterson, 1985: The volume transport of the Antarctic Circumpolar Current from bottom pressure measurements. *J. Phys. Oceanogr.,* **15,** 810–816.

Wyrtki, K., 1971: *Oceanographic Atlas of the International Indian Ocean Expedition.* National Science Foundation NSF-IOE-1, 531 pp.

Yu, T.-W., and R. D. McPherson, 1984: Global data assimilation experiments with scatterometer winds from Seasat-A. *Mon. Wea. Rev.,* **112,** 368–376.